

SYSTEMATIC STUDY OF THE PEAK ENERGY OF THE BROAD-BAND GAMMA-RAY BURST SPECTRA

DAISUKE KATSUKURA,¹ TAKANORI SAKAMOTO,² MAKOTO TASHIRO,¹ AND YUKIKATSU TERADA¹

¹*Department of Physics, Saitama University, Shimo-Okubo, Sakura-ku, Saitama, 338-8570, Japan*

²*Department of Physics and Mathematics, College of Science and Engineering, Aoyama Gakuin University, 5-10-1 Fuchinobe, Chuo-ku, Sagamihara-shi, Kanagawa 252-5258, Japan*

(Received June 25, 2019; Revised December 5, 2019; Accepted December 7, 2019)

Submitted to ApJ

ABSTRACT

We have performed a systematic study of Gamma-Ray Bursts (GRBs), which have various values in the peak energy of the νF_ν spectrum of the prompt emission, E_{peak} , observed by *Swift*/BAT and *Fermi*/GBM, investigating their prompt and X-ray afterglow emissions. We cataloged the long-lasting GRBs observed by the *Swift* between 2004 December and 2014 February in 3 categories according to the classification by Sakamoto et al. (2008): X-Ray Flashes (XRFs), X-Ray Rich GRBs (XRRs), and Classical GRBs (C-GRBs). We then derived $E_{\text{peak}}^{\text{obs}}$, as well as $E_{\text{peak}}^{\text{src}}$ if viable, of the *Swift* spectra of their prompt emission. We also analyzed their X-Ray afterglows and found the trend that the GRB events with a lower $E_{\text{peak}}^{\text{src}}$, i.e. softer GRBs, are fainter in the 0.3–10 keV X-ray luminosity and decay more slowly than harder GRBs. The intrinsic event rates of the XRFs, XRRs, and C-GRBs were calculated, using the *Swift*/BAT trigger algorithm. That of either of the XRRs and XRFs is larger than that of the C-GRBs. If we assume that the observational diversity of E_{peak} is explained with the off-axis model (Yamazaki et al. 2002, 2004), these results yield the jet half-opening angle of $\Delta\theta \sim 0.3^\circ$, and the variance of the observing angles $\theta_{\text{obs}} \lesssim 0.6^\circ$. This implies that the tiny variance of the observing angles of $\lesssim 0.6^\circ$ would be responsible for the E_{peak} diversity observed by *Swift*/BAT, which is unrealistic. Therefore, we conclude that the E_{peak} diversity is not explained with the off-axis model, but is likely to originate from some intrinsic properties of the jets.

Keywords: gamma rays: bursts X-rays: bursts

1. INTRODUCTION

The Gamma-Ray Bursts (GRBs) whose prompt emission lasts over 2 seconds are called a long GRBs. According to the widely accepted model of the long GRB, when a massive star dies and prompts a supernova, a black hole and ultra-relativistic jets are formed and then a long GRB may be observed if the jets point to us (Bloom et al. 1999; Woosley et al. 2006). The parameter E_{peak} , which is the peak energy of a νF_ν spectrum, indicates the general spectral property of GRBs. Past observations with *High Energy Transient Explorer 2* (*HETE*-2) showed that E_{peak} is distributed over a broad energy band from keV to MeV (Sakamoto et al. 2004). Notably, the GRBs observed by *HETE*-2 were

classified with following 3 categories in the basis of their softness ratio. They are classical GRBs (C-GRBs), X-ray rich GRBs (XRRs) and X-ray flushes (XRFs; Heise et al. 2003; Barraud et al. 2003; Sakamoto et al. 2005), in descending order of softness ratio. The three kinds of bursts are thought to be based on a unified jet picture (Lamb et al. 2005). Various theoretical models have been proposed to explain the emission process of XRFs and the mechanism generating 2–3 orders of diversity in E_{peak} , including, for example, a high redshift GRB model (Heise et al. 2003), dirty fireball model (Dermer et al. 1999; Rossi et al. 2002), GRB jets with a small contrast of Lorentz factors (Barraud et al. 2005), off-axis jet model (Yamazaki et al. 2002, 2004), and variable opening-angle model (Lamb et al. 2005). The validity of these models have been discussed in conjunction with the observed data by *CGRO*/BATSE (e.g., Paciesas et al. 1999; Kaneko et al. 2006) and *HETE*-2

(e.g., Barraud et al. 2003; Sakamoto et al. 2005). However, the information of the prompt emissions in the available data was insufficient to derive a definite conclusion about the emission mechanism of the long GRBs.

The theoretical models to explain the diversity of E_{peak} are broadly classified into two genres: (1) E_{peak} varies intrinsically from XRF to GRB, and (2) it originates mostly in the geometrical effect, while the intrinsic diversity is limited. One of the more accepted models for the latter is the off-axis model [e.g., Yamazaki et al. (2002, 2004)]. The off-axis model explains well at least the smaller end of E_{peak} . It also expects the afterglow light-curve to include a rising part, which originates in a weak and relativistic beaming effect accompanying the deceleration of the jet when the observer sees the jet off-axis. Thus, any observational relation between E_{peak} in the prompt emissions and afterglow light-curves (e.g., X-ray luminosity and temporal decay index), if found, would give a key to constrain the theoretical model.

In recent years, the *Neil Gehrels Swift Observatory* (Gehrels et al. 2004) has been observing the early GRB afterglows in multi-wavelengths from optical to X-ray bands since its launch in 2004. Sakamoto et al. (2008) conducted the first systematic study with the early *Swift* data with regard to the above-mentioned point and suggested that the X-ray luminosity (0.3–10 keV) of small E_{peak} events is lower than that of higher E_{peak} events. However, the number of samples in their study was very limited.

In this paper, we report the results of our systematic analysis of prompt and afterglow emissions of long GRBs observed by *Swift* between 2004 December and 2014 February. We handle them in three categories, following the classification criteria of Sakamoto et al. (2008): XRFs, XRRs and C-GRBs. In §2, we describe the samples of GRBs observed by *Swift* Burst Alert Telescope (BAT; Barthelmy et al. 2005) and then the analysis methods of the prompt emission by *Swift*/BAT and the broad-band afterglows observed by *Swift* X-Ray Telescope (XRT; Burrows et al. 2005a) and optical telescopes on the ground. In §3, we explain about details of our samples which were used for analysis of the prompt emissions and afterglows. In §4 and §5, we show the results of the systematic analysis of the prompt emissions and afterglows, respectively. In §6, we calculate the intrinsic event rates of the XRFs, XRRs, and C-GRBs, using the simulator of the *Swift*/BAT flight-trigger algorithm (Lien et al. 2014; Graff et al. 2016), and then discuss the consistency of theoretical models generating 2–3 orders of diversity of E_{peak} on the basis of the results of prompt emissions, afterglow emissions, and total numbers of the three classes of GRBs in the whole

universe per year, before summarizing our results in §7. Throughout this paper, the cosmological parameters of $\Omega_m = 0.274$, $\Omega_\Lambda = 0.726$, $H_0 = 70.5 \text{ km s}^{-1} \text{ Mpc}^{-1}$ (Spergel et al. 2007) are adopted. Error bars are in the 90% confidence level unless noted otherwise.

2. ANALYSIS

2.1. Classifying the GRBs observed by *Swift*

We classified the 750 long GRBs observed by *Swift* between 2004 December and 2014 February into three categories with the classification method by Sakamoto et al. (2008): XRFs, XRRs and C-GRBs. The classification uses the ratio of the fluences between 25–50 keV ($S_{25-50\text{keV}}$) and 50–100 keV ($S_{50-100\text{keV}}$), as follows.

$$\begin{aligned} S_{25-50\text{keV}}/S_{50-100\text{keV}} &\leq 0.72 \text{ (C - GRB)} \\ 0.72 < S_{25-50\text{keV}}/S_{50-100\text{keV}} &\leq 1.32 \text{ (XRR)} \\ S_{25-50\text{keV}}/S_{50-100\text{keV}} &> 1.32 \text{ (XRF)} \end{aligned} \quad (1)$$

We derived the fluences from the best-fit model of the X-ray spectra presented in Lien et al. (2016) (hereafter BAT3 catalog), and used them for classification. Our samples for the spectral analysis are long GRBs of which T_{90} in the BAT3 catalog are longer than 2 sec. Table 1 summarizes the number of GRBs and spectral samples for each class.

2.2. Spectral analysis of the prompt emissions

2.2.1. *Swift*/BAT data analysis

All the event data observed by *Swift*/BAT were retrieved from HEASARC at NASA Goddard Space Flight Center. The standard BAT software (HEADAS 6.15.1) and the latest calibration database (CALDB: 2009-01-30) at the time of analysis were used. First, we generated the time-averaged spectra (PHA) from the event data during t_{100} ¹, using the `batgrbproduct` pipeline. Then, systematic errors were added to each spectral data with the command `batupdatephawk`. The energy response functions were generated with the command `batdrmgen`. The command performed the calculation for a fixed single incident angle of the source and we achieved the data of the function if *Swift* was stationary during the t_{100} interval. As for the data for which the spacecraft slewed during the interval, we generated the response function for every 5 sec. The counts in each spectrum were weighted-averaged according to the photon count of every 5 sec, using the `addrmf` command (Sakamoto et al. 2008). For the sources classified as C-GRBs, we combined the *Swift*/BAT data and the data observed by the

¹ Time interval from 0% to 100% of the total burst fluence

Gamma-ray Burst Monitor (GBM; Meegan et al. 2009) onboard *Fermi*, because E_{peak} of those GRBs are expected to lie above the energy range of the *Swift*/BAT (15–150 keV). We also analyzed some XRRs by combining the BAT data with GBM data if E_{peak} value of the XRRs were not constrained by following analysis using only the data of Swift/BAT.

Finally, we performed model fitting of each spectrum, using `xspec`. We used 4 models to fit the spectra: a single power-law (PL), a PL with an exponential cut-off (CPL), Band function (Band 1993), and constrained Band function (C-Band; Sakamoto et al. 2004). Hereafter, the chi-squares of PL, CPL, and Band function are referred to as χ^2_{PL} , χ^2_{CPL} , and χ^2_{Band} , respectively. The procedure of the spectrum analysis and our criteria to decide the best-fit model are as follows.

1. The spectral data are fitted by the following models in the order of PL (two free parameters), CPL (three free parameters), and Band function (four free parameters).
2. We choose, as the best-fit model,
 - (a) PL if $\chi^2_{CPL} - \chi^2_{PL} \leq 6$, or
 - (b) CPL if $\chi^2_{CPL} - \chi^2_{PL} \geq 6$ and $\chi^2_{Band} - \chi^2_{CPL} \leq 6$, or
 - (c) Band function if $\chi^2_{CPL} - \chi^2_{PL} \geq 6$ and $\chi^2_{Band} - \chi^2_{CPL} \leq 6$.
3. If the spectrum is best-fitted by PL and if its photon index $\Gamma_{PL} < -2$, we fit the spectrum further with the C-Band model and give a tighter constraint on the value of E_{peak} .

2.2.2. *Fermi*/GBM data analysis

We retrieved time-tagged event data (TTE) of some of the XRRs and all the C-GRBs, corresponding to our *Swift*/BAT samples, observed by *Fermi*/GBM from HEASARC at NASA Goddard Space Flight Center. *Fermi* science tools version V10r0p5 were used for data reduction. *Fermi*/GBM has 12 NaI detectors and 2 BGO detectors, which are numbered 0–11 for NaI and 0–1 for BGO. We selected two NaI detectors and one BGO detector with the following criteria.

1. We choose the NaI detectors with source angles $\leq 60^\circ$ (Gruber et al. 2014).
2. We make the light curves for those event data, using the `gtbin` command.
3. The background is estimated from the fitting result of the pre- and post-burst light curve data with polynomial functions (χ^2 minimization) (see the following paragraph for detail).

4. We generate the background-subtracted light curves and select two NaI detectors the data of which have the highest signal-to-noise (SN) ratios.

5. If the selected NaI detector is one of 0–5, we use BGO-0 data, or otherwise BGO-1 data.

The exposure of the spectrum of the foreground object was chosen to be t_{100} obtained by *Swift*/BAT. The energy response functions were taken from the public archive of *Fermi* Science Data Center. The background (Item 3 in the list above) was estimated from the result of the model fitting; a pair of the 1000s light-curves before and after the event, i.e., one from 1000 seconds before the BAT trigger and the other for 1000 seconds after the end of BAT t_{100} , generated from the CSPEC data, for each channel were fitted with 1–4th-order polynomial functions, and then the best-fit model was incorporated into the burst time-intervals.

We performed joint spectral analysis with the *Swift*/BAT and *Fermi*/GBM data to better constrain the spectral parameters for the hard GRBs. The energy ranges used in the spectral analysis were 8–1000 keV for NaI and 0.3–38 MeV for BGO (Gruber et al. 2014). In the simultaneous spectral fitting, a constant factor to the model for each dataset relative to the *Swift*/BAT data was introduced to take into account the uncertainty in the cross-instrumental calibration. The criteria to decide the best-fit model were the same as in section 2.2.1

2.3. Analysis of afterglows

2.3.1. X-Ray afterglow

The X-ray afterglow samples are limited to the GRBs that have the well-constrained E_{peak} in our sample, following the analyses described in the previous section. We retrieved X-ray afterglow light-curves (in the 0.3–10 keV band) through the UK *Swift* Science Data Centre (Evans et al. 2009, <http://www.swift.ac.uk>). In some GRBs, X-ray flares (Zang et al. 2006) occurred during the shallow decay phase in X-ray afterglow, which were excluded by eye inspection from our sample. We made the 0.3–10 keV light curves in luminosity ($L_{0.3-10\text{keV}}$) for the events with known redshifts in the analyzed samples, using equation (2):

$$L_{0.3-10\text{keV}} = 4\pi d_L^2 (1+z)^{-\Gamma-2} F_{0.3-10\text{keV}}, \quad (2)$$

where d_L and $F_{0.3-10\text{keV}}$ are the luminosity distance and the energy flux observed by *Swift*/XRT, respectively, and Γ is the photon index of the X-ray afterglow at the late-time phase, which is available in the UK *Swift* Science Data Centre. We then performed model fitting for X-ray energy flux and luminosity light-curves with

the models of a simple power-law (PL), a PL with one temporal break (BPL1), a PL with two temporal breaks (BPL2), and a PL with three temporal breaks (BPL3) in this order until the resultant χ^2 did not show an improvement greater than 2. Accordingly, the X-ray luminosity ($L_{0.3-10\text{keV},200\text{s}}$) and the temporal decay index ($\Gamma_{200\text{s}}$) at 200 seconds after the trigger at the GRB rest frame were derived. Some GRBs were in the steep decay phase in the $\Gamma_{200\text{s}}$ interval, in which case the temporal index in the period following the shallow decay phase was extrapolated to the epoch of the 200 seconds and the values of $L_{0.3-10\text{keV},200\text{s}}$ and $\Gamma_{200\text{s}}$ were derived at that epoch in the same way as described in Racusin et al. (2016).

2.3.2. Optical afterglow

To analyze the optical afterglow, we collected the optical data published in Gamma-ray burst Coordinate Network (GCN) and literature. Table 7 summarizes the references of our samples. The galactic extinctions are corrected according to Schlegel et al. (1998).

3. SAMPLE OF GRBS

3.1. Results of classification of the *Swift* GRBs

We cataloged in Table 1 the long GRBs observed by *Swift* between 2004 December and 2014 February with a classification of XRFs, XRRs, and C-GRBs based on equation 2. Figure 1 shows the distribution of fluence ratio between 25–50 keV and 50–100 keV ($S_{25-50\text{keV}}/S_{50-100\text{keV}}$). We found that XRFs, XRRs, and C-GRBs are distributed continuously in a single peak.

Table 1. Numbers of raw events, those analyzed for spectra and known redshift events for XRFs, XRRs, and C-GRBs

Class	Events	Analyzed samples	Redshift samples
XRF	28 (3.7%)	26	11
XRR	452 (60.2%)	41	20
C-GRB	270 (36.0%)	13	9
sum	750	80	40

3.2. Analyzed samples

Because a measurement of the prompt emission parameters (e.g. E_{peak}) is crucial in this study, we select the samples of the well constrained spectral parameters

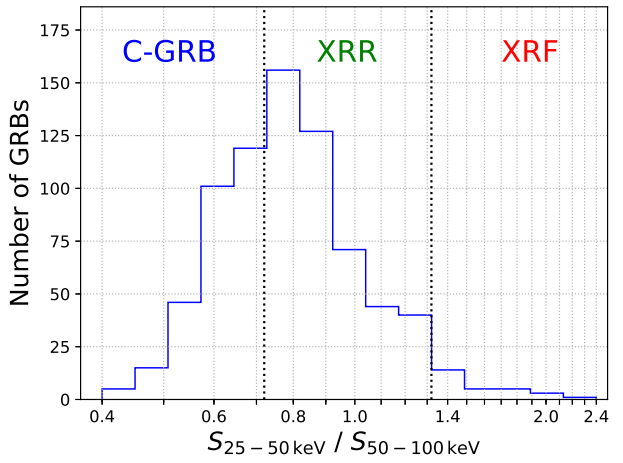


Figure 1. GRB number histogram for $S_{25-50\text{keV}}/S_{50-100\text{keV}}$. XRFs, XRRs, and C-GRBs are distributed continuously from the single peak.

of the prompt emission. The samples are also required to have a good quality data of *Swift*/XRT. The spectral analysis for XRFs, XRRs, and C-GRBs were performed in the basis of the method described in 2.2.1.

Since the number of samples of XRFs were limited, we selected all XRFs with a good quality data of *Swift*/XRT. The XRR samples were selected in descending order of the peak flux (15–150 keV). In case E_{peak} was not constrained by the *Swift*/BAT data alone, we performed joint spectral analysis of *Swift*/BAT and *Fermi*/GBM data if they were commonly detected. We continued the analysis until the samples of XRRs were equivalent to fifty. Since nine XRRs do not have a good quality of *Swift*/XRT data, the total number of the analyzed samples for XRRs are 41. As for C-GRBs, it is expected that those of the E_{peak} exceed the upper boundary the BAT energy band of 150 keV (Sakamoto et al. 2008). Therefore, the spectral analysis was performed for the events observed by both *Swift*/BAT and *Fermi*/GBM. Because of the requirement of *Fermi*/GBM data for the analysis of C-GRBs, the total numbers of the analyzed samples of C-GRBs were significantly reduced to 13.

We also constructed the samples with redshifts from the analyzed samples. Table 1 summarized the numbers of our entire samples, analyzed samples and redshift samples for XRFs, XRRs, and C-GRBs.

4. RESULTS OF THE PROMPT EMISSIONS

4.1. Spectral analysis

Table 2 summarizes the results of the spectral fitting with the CPL, Band function, and C-Band models. Figure 2 shows the relation between the fluence

ratio $S_{25-50\text{keV}}/S_{50-100\text{keV}}$ and $E_{\text{peak}}^{\text{obs}}$, which is defined as the E_{peak} in the observer's frame. The theoretical curve of $S_{25-50\text{keV}}/S_{50-100\text{keV}}$ in the case of the low energy spectral index $\alpha = -1$ and the high energy spectral index $\beta = -2.5$ for the Band function is overlaid in the figure (dashed line). The value of $S_{25-50\text{keV}}/S_{50-100\text{keV}}$ depends on $E_{\text{peak}}^{\text{obs}}$ strongly, whereas it is not a strong function of the values of α and β . Therefore, in the energy range of *Swift/BAT*, this classification according to the fluence ratio is practically equivalent to that according to $E_{\text{peak}}^{\text{obs}}$. In addition, we note that the $E_{\text{peak}}^{\text{obs}}$ of XRFs, XRRs, and C-GRBs are distributed continuously from a few to hundreds of keV.

Figure 3 shows comparison of the fluence ratios based on our spectral modelling (R_{mod}) with those based on the spectral fits of the BAT3 catalog (R_{BAT3}). R_{mod} tends to be slightly larger, especially in XRRs, than R_{BAT3} . GRB080916A and GRB080714 change to XRR in the basis of classification using R_{mod} . They are, however, consistent to be C-GRB considering their error regions. Additionally, most of analyzed sample do not deviate significantly from $R_{\text{mod}} = R_{\text{BAT3}}$. Thus, the

tendency generated by the difference of modeling between BAT3 catalog and our analysis is negligible.

Figure 4 shows the energy fluence in the energy band of *Swift/BAT* (15–150 keV) versus $E_{\text{peak}}^{\text{obs}}$. The 15–150 keV fluence of the XRFs tends to be lower (dimmer) than those of the XRRs and C-GRBs.

The redshift (z), $E_{\text{peak}}^{\text{src}}$, and the total isotropic-equivalent radiated energy E_{iso} of our samples are summarized in table 3. Figure 5 shows the distribution of z and $E_{\text{peak}}^{\text{obs}}$. No clear trend of clustering of the *Swift/BAT* XRF population, especially towards the high redshift end, is observed, which contradicts the suggestion that the XRFs would be in high-redshift origin (Heise et al. 2001). Figure 6 shows the correlation, known as the Amati relation (Amati et al. 2002), between the rest-frame E_{peak} ($E_{\text{peak}}^{\text{src}}$) and E_{iso} . Our samples are consistent within the error with the relation derived from the best-fit result of Amati et al. (2006) for the $\pm 2\sigma$ region except for XRR130925A. Note that the figure also shows that our sample has the diversity for 2 and 3 orders of magnitude in $E_{\text{peak}}^{\text{src}}$ and E_{iso} , respectively.

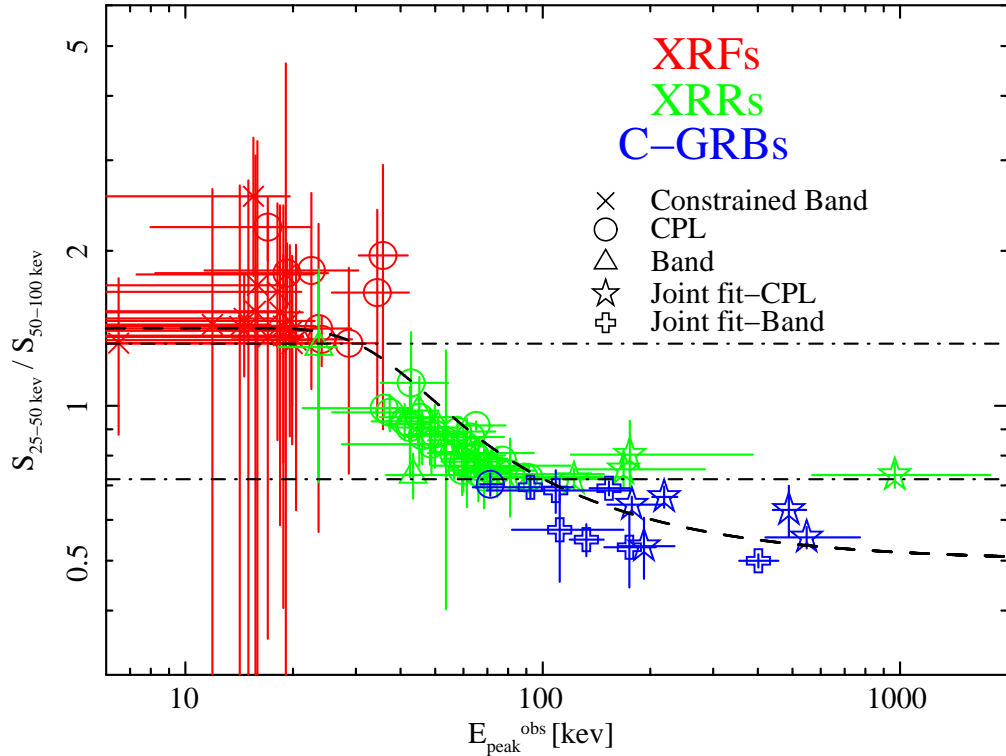


Figure 2. Fluence ratio $S_{25-50 \text{ keV}} / S_{50-100 \text{ keV}}$ versus $E_{\text{peak}}^{\text{obs}}$. Dashed line is the theoretical curve of the Band function for $\alpha = -1$ and the $\beta = -2.5$ (see text). The upper and lower dot-dashed lines are $S_{25-50 \text{ keV}} / S_{50-100 \text{ keV}}$ for $E_{\text{peak}}^{\text{obs}} = 30$ and 100 keV, respectively. The number of samples in this figure is $N = 80$.

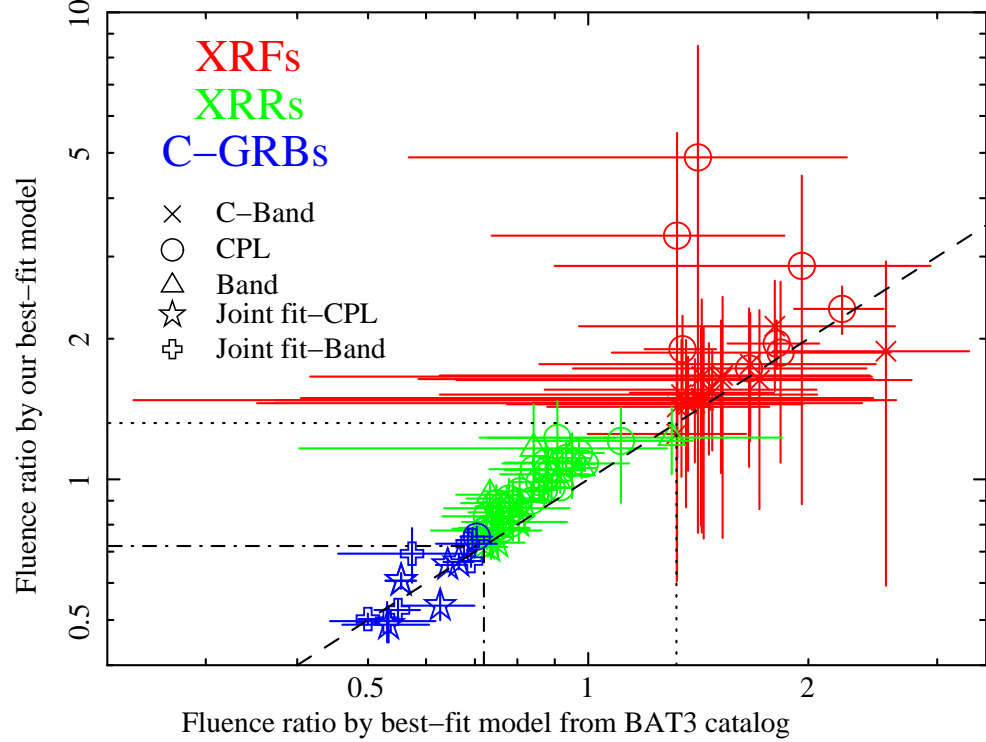


Figure 3. Comparison of the fluence ratios based on our spectral modelling (R_{mod}) with those based on the spectral fits of the BAT3 catalog (R_{BAT3}). The dashed line represents $R_{\text{mod}} = R_{\text{BAT3}}$. The dotted and the dot-dashed lines are $R_{\text{mod}}, R_{\text{BAT3}} = 1.32$ and $R_{\text{mod}}, R_{\text{BAT3}} = 0.72$, respectively. The number of samples in this figure is $N = 80$.

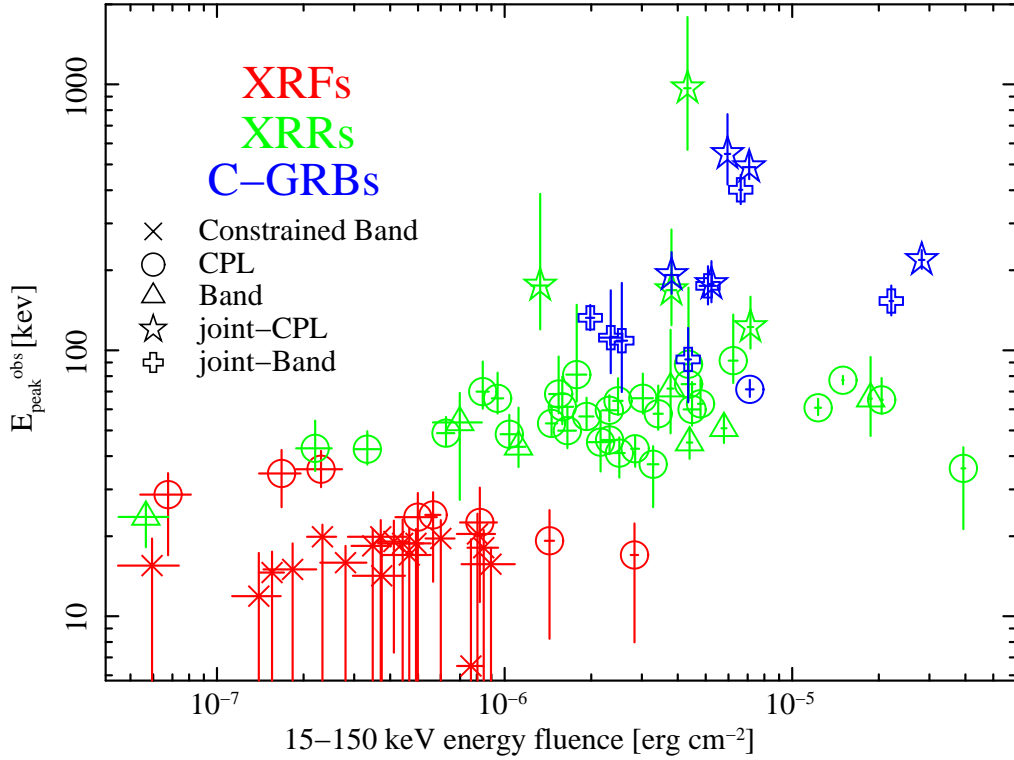


Figure 4. $E_{\text{peak}}^{\text{obs}}$ versus energy fluence in the energy band of Swift/BAT (15–150 keV). The number of samples in this figure is $N = 80$.

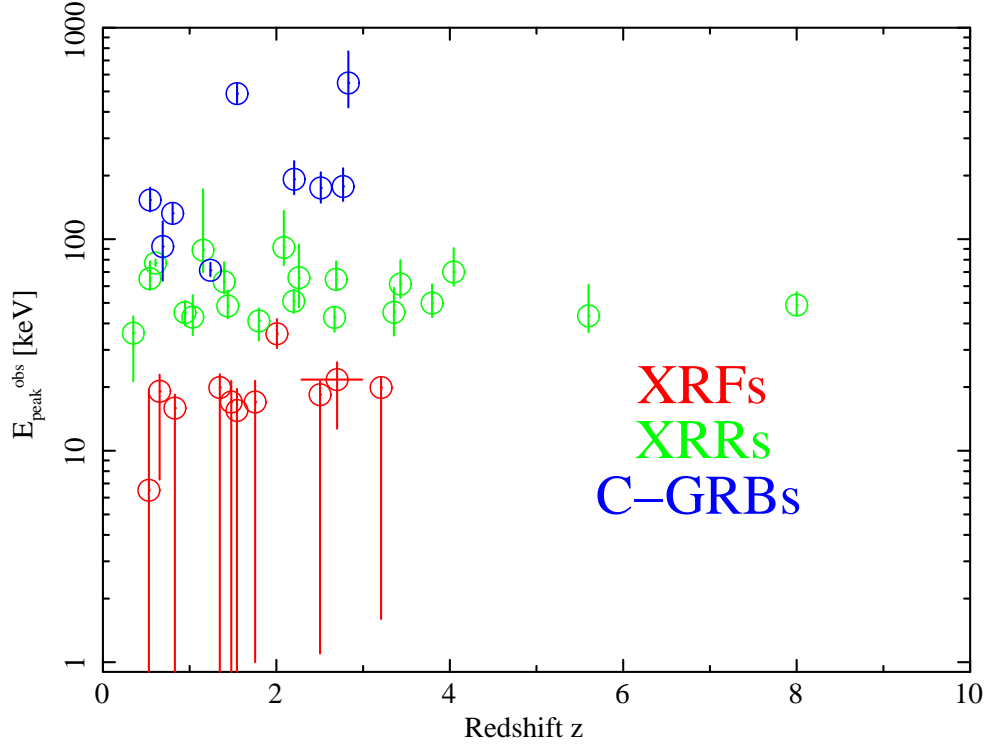


Figure 5. Distribution of z and $E_{\text{peak}}^{\text{obs}}$. The number of samples in this figure is $N = 40$.

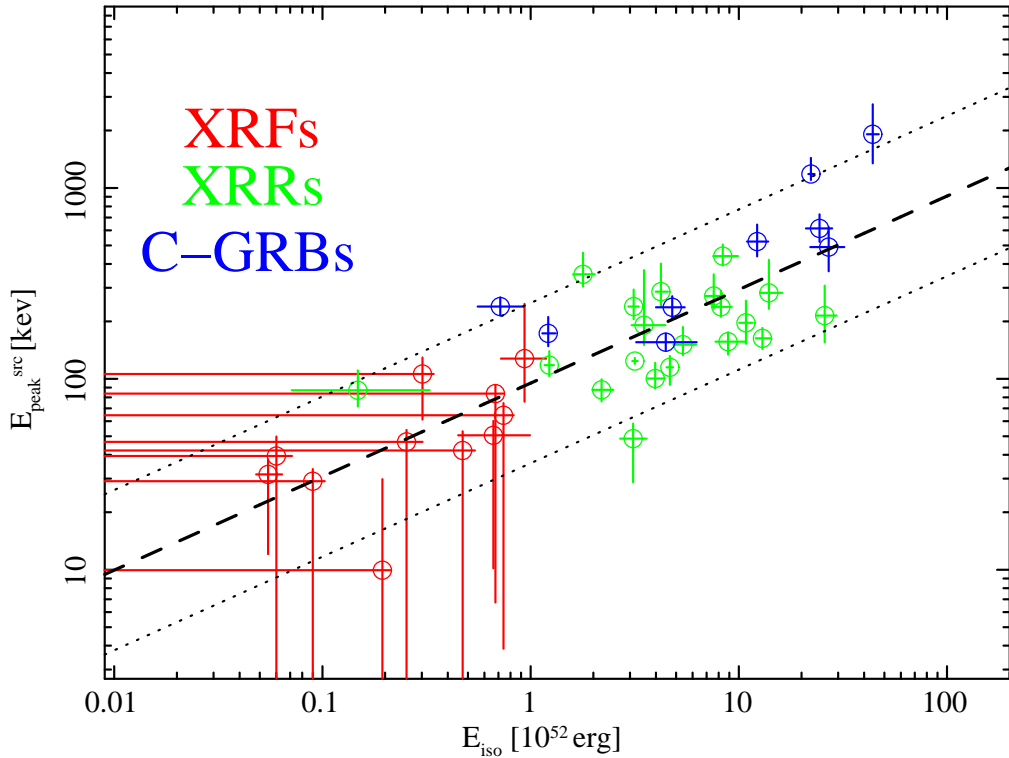


Figure 6. Scatter plot of $E_{\text{peak}}^{\text{src}}$ versus E_{iso} for our samples. The dashed line represents the best-fit power-law ($E_{\text{peak}}^{\text{src}} = 95 \times (E_{\text{iso}}/10^{52})^{0.49}$) and the two dotted lines delineate the region corresponding to $\pm 2\sigma$, which are derived from Amati et al. (2006). The number of samples in this figure is $N = 40$.

Table 2. Summary of our spectral fitting results with the CPL, Band function, and C-Band models.

Events	α^a	β^b	$E_{\text{peak}}^{\text{obs}}$ (keV)	$\chi^2/\text{d.o.f.}$	ratio ^c	fluence ^d	constant factor ^e			model ^f
							GBM-NaI(1)	GBM-NaI(2)	GBM-BGO	
XRF050406	> -1.48	...	$28.7^{+5.7}_{-11.7}$	77.42/58	$1.32^{+0.53}_{-0.58}$	$0.778^{+0.018}_{-0.017}$	CPL
XRF050416A	...	$-3.08^{+0.21}_{-0.23}$	$19.1^{+3.8}_{-11.1}$	59.98/58	$2.26^{+0.76}_{-0.86}$	$4.13^{+0.55}_{-0.53}$	C-Band
XRF050819	...	$-2.69^{+0.27}_{-0.30}$	$18.4^{+2.9}_{-17.1}$	58.49/58	$1.56^{+0.50}_{-0.55}$	$3.48^{+0.56}_{-0.53}$	C-Band
XRF050824	...	$-2.72^{+0.34}_{-0.39}$	< 18.4	55.82/58	$1.73^{+0.71}_{-0.82}$	$2.78^{+0.53}_{-0.50}$	C-Band
XRF060219	...	$-2.50^{+0.29}_{-0.33}$	$18.8^{+4.3}_{-17.1}$	64.84/58	$1.44^{+0.51}_{-0.55}$	$4.40^{+0.81}_{-0.78}$	C-Band
XRF060428B	...	$-2.81^{+0.24}_{-0.26}$	< 21.1	64.77/58	$1.72^{+0.48}_{-0.52}$	$8.441^{+1.07}_{-1.03}$	C-Band
XRF060923B	...	$-2.53^{+0.23}_{-0.25}$	$18.8^{+2.5}_{-17.2}$	55.17/58	$1.39^{+0.35}_{-0.37}$	$4.90^{+0.63}_{-0.62}$	C-Band
XRF060926	...	$-2.54^{+0.21}_{-0.23}$	$19.9^{+2.2}_{-18.2}$	59.14/58	$1.41^{+0.34}_{-0.36}$	$2.32^{+0.28}_{-0.27}$	C-Band
XRF070330	$0.27^{+1.79}_{-1.26}$...	$30.4^{+7.8}_{-8.7}$	64.72/58	$1.66^{+0.76}_{-0.71}$	$1.67^{+0.26}_{-0.30}$	CPL
XRF070714A	...	$-2.62^{+0.22}_{-0.21}$	< 17.5	61.10/58	$1.48^{+0.32}_{-0.34}$	1.55 ± 0.16	C-Band
XRF080218B	> -1.44	...	< 29.1	48.44/58	1.41 ± 0.84	$4.81^{+0.94}_{-0.82}$	CPL
XRF080520	...	$-2.80^{+0.41}_{-0.47}$	$15.5^{+4.1}_{-14}$	55.46/58	$2.11^{+1.22}_{-1.54}$	$0.59^{+0.15}_{-0.14}$	C-Band
XRF081007	...	$-2.52^{+0.19}_{-0.21}$	< 19.5	58.28/58	$1.34^{+0.28}_{-0.29}$	$7.61^{+0.82}_{-0.81}$	C-Band
XRF100425A	...	$-2.48^{+0.29}_{-0.32}$	$17.0^{+4.4}_{-16}$	50.20/58	$1.35^{+0.49}_{-0.53}$	$4.64^{+0.91}_{-0.86}$	C-Band
XRF110319A	$-1.39^{+0.48}_{-0.44}$...	$19.2^{+5.8}_{-10}$	53.33/58	1.82 ± 0.20	14.3 ± 0.7	CPL
XRF110808A	...	$-2.27^{+0.38}_{-0.43}$	$19.9^{+3.1}_{-19}$	58.71/58	1.321 ± 0.32	$3.69^{+0.88}_{-0.84}$	C-Band
XRF111129A	...	$-2.66^{+0.36}_{-0.42}$	$15.0^{+3.8}_{-14}$	52.47/58	$1.44^{+0.59}_{-0.66}$	$1.82^{+0.40}_{-0.37}$	C-Band
XRF120116A	$-1.36^{+0.47}_{-0.43}$...	$17.0^{+5.3}_{-9.0}$	47.85/58	2.11 ± 0.22	28.8 ± 1.3	CPL
XRF120724A	...	$-2.56^{+0.25}_{-0.28}$	$20.4^{+3.9}_{-16}$	52.90/58	$1.35^{+0.39}_{-0.41}$	$8.00^{+1.25}_{-1.22}$	C-Band
XRF120816A	...	$-2.54^{+0.34}_{-0.40}$	< 19.6	55.78/58	$1.42^{+0.57}_{-0.61}$	$3.73^{+0.79}_{-0.76}$	C-Band
XRF121108A	> -2.15	...	$22.5^{+8.3}_{-12.2}$	46.58/58	1.83 ± 0.76	$8.28^{+1.38}_{-1.17}$	CPL
XRF121212A	...	$-2.56^{+0.37}_{-0.42}$	$11.9^{+5.4}_{-11.0}$	57.08/58	$1.42^{+0.56}_{-0.63}$	$1.39^{+0.28}_{-0.26}$	C-Band
XRF130608A	...	$-2.74^{+0.39}_{-0.46}$	$15.7^{+2.4}_{-15.0}$	55.47/58	$1.54^{+0.67}_{-0.76}$	$8.90^{+1.96}_{-1.84}$	C-Band
XRF130612A	> -2.0	...	$35.7^{+6.2}_{-5.2}$	48.28/58	$1.96^{+0.98}_{-1.06}$	$8.90^{+1.96}_{-1.84}$	CPL
XRF130812A	$-1.14^{+0.65}_{-0.57}$...	$24.1^{+5.2}_{-10.6}$	63.24/58	1.35 ± 0.15	6.27 ± 0.36	CPL
XRF140103A	...	$-2.64^{+0.22}_{-0.24}$	$19.6^{+3.4}_{-16.0}$	72.39/58	$1.51^{+0.36}_{-0.38}$	$6.00^{+0.71}_{-0.70}$	C-Band
XRR050318	$-1.08^{+0.45}_{-0.41}$...	$48.4^{+8.9}_{-6.0}$	54.37/58	$1.04^{+0.12}_{-0.11}$	$10.4^{+0.8}_{-0.7}$	CPL

Table 2 continued

Table 2 (continued)

Events	α^a	β^b	$E_{\text{peak}}^{\text{obs}}$ (keV)	$\chi^2/\text{d.o.f.}$	ratio ^c	fluence ^d	constant factor ^e			model ^f
							GBM-NaI(1)	GBM-NaI(2)	GBM-BGO	
XRR050410	$-0.829^{+0.39}_{-0.36}$...	74.6^{+20}_{-10}	60.39/58	0.779 ± 0.068	43.5 ± 2.5	CPL
XRR050525A	$-1.01^{+0.10}_{-0.10}$...	$77.1^{+3.0}_{-2.6}$	20.61/58	0.792 ± 0.019	151 ± 2	CPL
XRR050915B	$-1.39^{+0.31}_{-0.29}$...	$57.7^{+15}_{-7.5}$	57.63/58	0.948 ± 0.058	34.0 ± 1.4	CPL
XRR060206	$-1.06^{+0.33}_{-0.31}$...	$70.0^{+20}_{-9.7}$	58.63/58	0.809 ± 0.061	8.42 ± 0.44	CPL
XRR060707	$-0.602^{+0.680}_{-0.590}$...	$61.3^{+18}_{-8.7}$	61.65/58	$0.846^{+0.123}_{-0.122}$	15.8 ± 1.5	CPL
XRR060825	$-1.07^{+0.32}_{-0.29}$...	$66.0^{+16}_{-8.2}$	55.92/58	$0.843^{+0.058}_{-0.057}$	$9.55^{+0.47}_{-0.47}$	CPL
XRR060927	$0.37^{+1.5}_{-1.1}$	$-2.01^{+0.17}_{-0.30}$	$43.4^{+17}_{-7.0}$	63.93/57	$0.810^{+0.068}_{-0.067}$	11.2 ± 0.7	Band
XRR061222B	$-1.22^{+0.60}_{-0.53}$...	45.2^{+13}_{-10}	63.24/58	0.970 ± 0.129	22.7 ± 1.8	CPL
XRR070612B	$-0.902^{+0.54}_{-0.48}$...	81.0^{+67}_{-16}	39.05/58	0.736 ± 0.085	18.2 ± 1.4	CPL
XRR070721A	> -0.31	$-3.33^{+0.76}_{-2.81}$	$23.6^{+2.9}_{-5.5}$	49.31/57	$1.27^{+0.54}_{-0.59}$	$0.730^{+0.182}_{-0.172}$	Band
XRR071010B	$-1.22^{+0.53}_{-0.35}$	< -2.18	$45.0^{+6.1}_{-5.9}$	31.97/57	0.977 ± 0.037	46.2 ± 1.0	Band
XRR080207	$-1.17^{+0.26}_{-0.25}$...	91.5^{+44}_{-16}	53.43/58	0.737 ± 0.039	64.0 ± 2.1	CPL
XRR080212	$-0.274^{+0.67}_{-0.58}$...	$66.0^{+15}_{-8.2}$	51.93/58	$0.741^{+0.090}_{-0.089}$	30.1 ± 2.6	CPL
XRR080603B	$-1.16^{+0.29}_{-0.27}$...	$64.6^{+13}_{-7.3}$	61.63/58	$0.849^{+0.051}_{-0.051}$	24.6 ± 1.1	CPL
XRR081128	$-1.03^{+0.47}_{-0.42}$...	$46.0^{+6.5}_{-5.3}$	34.14/58	1.03 ± 0.11	23.4 ± 1.6	CPL
XRR081221	$-1.18^{+0.51}_{-0.30}$...	65.8^{+28}_{-18}	31.03/58	0.816 ± 0.021	189 ± 3	CPL
XRR090423	$-0.803^{+0.52}_{-0.46}$...	$48.8^{+7.4}_{-5.2}$	41.19/58	$0.980^{+0.110}_{-0.108}$	$6.24^{+0.46}_{-0.45}$	CPL
XRR090429B	$-0.587^{+0.82}_{-0.68}$...	$42.5^{+7.1}_{-5.3}$	31.04/58	$1.15^{+0.22}_{-0.20}$	$3.29^{+0.36}_{-0.34}$	CPL
XRR090531A	$-0.874^{+0.45}_{-0.41}$...	68.5^{+26}_{-10}	41.64/58	$0.785^{+0.082}_{-0.081}$	15.4 ± 1.2	CPL
XRR090813	$-1.57^{+0.12}_{-0.14}$...	175^{+212}_{-55}	90.70/86	$0.812^{+0.091}_{-0.091}$	13.3 ± 1.0	$1.22^{+0.11}_{-0.10}$	$1.31^{+0.13}_{-0.12}$	< 6.58	joint-CPL
XRR090912	$-0.936^{+0.46}_{-0.42}$...	$59.9^{+16}_{-7.9}$	38.31/58	$0.841^{+0.084}_{-0.083}$	44.8 ± 3.1	CPL
XRR100615A	$-1.56^{+0.20}_{-0.19}$...	$63.0^{+14}_{-7.4}$	35.55/58	$0.910^{+0.034}_{-0.034}$	49.2 ± 1.1	CPL
XRR100621A	$-1.72^{+0.13}_{-0.13}$...	$65.1^{+13}_{-7.5}$	32.02/58	0.931 ± 0.024	206 ± 3	CPL
XRR101024A	$-1.09^{+0.35}_{-0.32}$...	$53.1^{+7.4}_{-5.3}$	53.08/58	0.924 ± 0.069	14.5 ± 0.7	CPL
XRR110411A	$-1.51^{+0.35}_{-0.32}$...	$37.3^{+6.3}_{-11}$	45.33/58	1.09 ± 0.08	33.0 ± 1.6	CPL
XRR110726A	$-0.622^{+1.023}_{-0.832}$...	$42.8^{+11.6}_{-7.7}$	56.53/58	$1.11^{+0.28}_{-0.27}$	$2.18^{+0.33}_{-0.30}$	CPL
XRR111022A	$-0.872^{+0.42}_{-0.38}$...	$56.4^{+9.9}_{-6.0}$	58.22/58	$0.877^{+0.076}_{-0.075}$	19.2 ± 1.2	CPL
XRR120102A	$-1.49^{+0.03}_{-0.04}$...	967^{+825}_{-399}	162.98/118	0.752 ± 0.035	43.2 ± 1.2	$1.29^{+0.07}_{-0.06}$	$1.00^{+0.07}_{-0.06}$	$2.40^{+1.65}_{-0.87}$	joint-CPL
XRR120326A	$-1.41^{+0.35}_{-0.32}$...	$41.1^{+6.0}_{-7.9}$	55.90/58	1.05 ± 0.08	25.2 ± 1.3	CPL
XRR120703A	$-1.34^{+0.14}_{-0.16}$...	168^{+116}_{-44}	132.04/118	0.754 ± 0.050	37.9 ± 1.6	$1.26^{+0.13}_{-0.12}$	1.26 ± 0.11	± 74.7	joint-CPL

Table 2 (continued)

Events	α^a	β^b	$E_{\text{peak}}^{\text{obs}}$ (keV)	$\chi^2/\text{d.o.f.}$	ratio ^c	fluence ^d	constant factor ^e			model ^f
							GBM-NaI(1)	GBM-NaI(2)	GBM-BGO	
XRR120802A	$-1.10^{+0.52}_{-0.46}$...	$49.9^{+11}_{-7.0}$	58.14/58	$0.953^{+0.109}_{-0.107}$	16.4 ± 1.3	CPL
XRR120811C	$-1.40^{+0.31}_{-0.29}$...	$42.7^{+5.2}_{-6.2}$	48.95/58	1.05 ± 0.06	28.5 ± 1.1	CPL
XRR120927A	$-0.556^{+0.42}_{-0.38}$...	$59.5^{+8.3}_{-5.4}$	57.34/58	$0.812^{+0.069}_{-0.069}$	23.1 ± 1.4	CPL
XRR121123A	$-0.917^{+0.22}_{-0.21}$...	$60.8^{+5.0}_{-3.7}$	57.43/58	$0.840^{+0.034}_{-0.034}$	124 ± 4	CPL
XRR121128A	$-1.02^{+0.45}_{-0.33}$	$-2.33^{+0.17}_{-0.76}$	$50.9^{+6.9}_{-6.1}$	33.21/57	$0.912^{+0.034}_{-0.034}$	58.3 ± 1.5	Band
XRR130627A	$0.32^{+1.69}_{-1.24}$	$-2.23^{+0.40}_{-0.61}$	53.6^{+30}_{-26}	60.28/57	$0.842^{+0.244}_{-0.246}$	$7.66^{+1.46}_{-1.44}$	Band
XRR130701A	$-1.11^{+0.39}_{-0.36}$...	88.7^{+83}_{-18}	59.58/58	$0.734^{+0.036}_{-0.036}$	43.8 ± 1.3	CPL
XRR130727A	$-1.14^{+0.56}_{-0.34}$	$-1.89^{+0.12}_{-0.25}$	71.8^{+47}_{-23}	54.12/57	$0.786^{+0.033}_{-0.033}$	38.4 ± 1.0	Band
XRR130925A	$-1.75^{+0.17}_{-0.17}$...	$36.0^{+7.2}_{-14}$	45.25/58	1.04 ± 0.03	403 ± 7	CPL
XRR140108A	$-1.32^{+0.12}_{-0.14}$...	122^{+36}_{-20}	135.82/112	0.720 ± 0.034	71.4 ± 1.8	$1.43^{+0.11}_{-0.11}$	$1.44^{+0.12}_{-0.11}$...	joint-CPL
GRB080714	$-1.11^{+0.43}_{-0.25}$	$-1.95^{+0.18}_{-0.31}$	$109^{+70.5}_{-39.0}$	84.08/85	0.678 ± 0.047	$25.5^{+1.2}_{-1.1}$	$1.55^{+0.16}_{-0.15}$	1.26 ± 0.13	$3.02^{+3.71}_{-1.77}$	joint-Band
GRB080804	$-0.56^{+0.16}_{-0.18}$...	192^{+42}_{-29}	93.80/81	0.531 ± 0.050	37.9 ± 2.1	$1.17^{+0.10}_{-0.09}$	$1.10^{+0.10}_{-0.09}$...	joint-CPL
GRB080916A	$-1.00^{+0.38}_{-0.19}$	$-2.06^{+0.22}_{-1.65}$	$92.4^{+29.0}_{-28.7}$	119.93/117	0.695 ± 0.034	42.2 ± 1.3	1.24 ± 0.09	1.29 ± 0.08	< 6.02	joint-Band
GRB081121	$-0.54^{+0.18}_{-0.16}$	$-2.14^{+0.17}_{-0.27}$	175^{+32}_{-26}	132.76/125	0.531 ± 0.059	50.8 ± 3.3	$1.24^{+0.10}_{-0.09}$	$1.10^{+0.10}_{-0.09}$	$1.59^{+0.54}_{-0.40}$	joint-Band
GRB081222	$-0.99^{+0.21}_{-0.14}$	$-1.97^{+0.18}_{-0.32}$	$130^{+35.7}_{-32.5}$	105.21/81	0.664 ± 0.022	52.2 ± 1.1	1.37 ± 0.06	1.15 ± 0.07	$3.08^{+6.01}_{-1.88}$	joint-Band
GRB090102	-0.99 ± 0.04	...	488^{+58}_{-48}	246.83/188	0.627 ± 0.051	70.6 ± 3.7	$1.24^{+0.07}_{-0.06}$	1.28 ± 0.07	$1.29^{+0.19}_{-0.17}$	joint-CPL
GRB090424	$-1.11^{+0.07}_{-0.06}$	$-2.22^{+0.16}_{-0.41}$	153^{+21}_{-18}	155.41/85	0.709 ± 0.024	218 ± 4	1.18 ± 0.03	1.15 ± 0.03	$1.18^{+0.96}_{-0.58}$	joint-Band
GRB090926B	$-0.43^{+0.26}_{-0.24}$...	$71.3^{+6.1}_{-4.5}$	50.77/58	0.704 ± 0.035	71.2 ± 2.4	CPL
GRB100816A	$-0.45^{+0.15}_{-0.14}$	$-2.22^{+0.22}_{-0.43}$	131^{+18}_{-14}	163.25/125	0.548 ± 0.033	19.5 ± 0.7	1.17 ± 0.07	1.14 ± 0.07	$1.23^{+0.93}_{-0.60}$	joint-Band
GRB110625A	-1.22 ± 0.04	...	219^{+19}_{-16}	221.12/114	0.675 ± 0.027	281 ± 7	1.19 ± 0.04	1.33 ± 0.04	$2.98^{+2.03}_{-1.62}$	joint-CPL
GRB110731A	-1.21 ± 0.06	...	548^{+225}_{-123}	162.41/118	0.554 ± 0.022	59.4 ± 1.4	2.10 ± 0.10	2.20 ± 0.12	$1.41^{+1.36}_{-0.98}$	joint-CPL
GRB121011A	$-1.01^{+0.37}_{-0.28}$	$-2.37^{+0.42}_{-2.06}$	112^{+57}_{-30}	118.51/85	0.555 ± 0.084	22.6 ± 2.1	$1.46^{+0.22}_{-0.19}$	$1.50^{+0.24}_{-0.22}$	$23.1^{+310.9}_{-21.9}$	joint-Band
GRB131229A	$-0.85^{+0.05}_{-0.04}$	$-2.46^{+0.27}_{-0.63}$	401^{+56}_{-47}	201.06/187	0.526 ± 0.020	68.9 ± 1.5	1.23 ± 0.04	1.25 ± 0.04	$1.33^{+0.21}_{-0.18}$	joint-Band

^aLow-energy spectral index^bHigh-energy spectral index^cFluence ratio of $S_{25-50\text{keV}}/S_{50-100\text{keV}}$ derived from the best-fit model.^dBAT 15–150-keV energy fluence in $10^{-7} \text{ erg cm}^{-2} \text{ s}^{-1}$ derived from the best-fit model.^eConstant factor relative to the BAT data.^fThe best-fit model.

Table 3. Summary of redshift, peak energy ($E_{\text{peak}}^{\text{src}} \equiv (1+z)E_{\text{peak}}^{\text{obs}}$), and equivalent isotropic energy (E_{iso}) of our samples.

Events	Redshift (z)	$E_{\text{peak}}^{\text{src}}$ [keV]	E_{iso} [10^{52} erg]
XRF050406	$2.7^{+0.29}_{-0.41}$	106^{+23}_{-45}	< 0.342
XRF050416A	0.6535	$31.6^{+6.3}_{-19}$	$0.0548^{+0.0092}_{-0.0067}$
XRF050819	2.5043	< 74.6	< 0.830
XRF050824	0.83	< 33.7	< 0.102
XRF060926	3.208	< 93.0	< 0.741
XRF080520	1.545	< 49.9	< 0.0714
XRF081007	0.5295	< 29.8	< 0.212
XRF100425A	1.755	< 53.1	< 0.540
XRF110808A	1.348	< 54.0	< 0.303
XRF120724A	1.48	$50.6^{+9.7}_{-40.4}$	$0.662^{+0.331}_{-0.214}$
XRF130612A	2.006	128^{+120}_{-52}	$0.934^{+0.253}_{-0.215}$
XRR050318	1.44	118^{+21}_{-14}	$1.23^{+0.06}_{-0.06}$
XRR050525A	0.606	$123^{+4.8}_{-4.1}$	$3.17^{+0.10}_{-0.09}$
XRR060206	4.045	352^{+110}_{-48}	$1.78^{+0.25}_{-0.18}$
XRR060707	3.43	271^{+81}_{-38}	$7.57^{+0.71}_{-0.66}$
XRR060927	5.6	286^{+120}_{-46}	$4.23^{+0.34}_{-0.24}$
XRR061222B	3.355	196^{+60}_{-44}	$10.8^{+0.8}_{-0.8}$
XRR071010B	0.947	$87.6^{+11.0}_{-11.0}$	$2.19^{+0.31}_{-0.21}$
XRR080207	2.0858	282^{+140}_{-49}	$13.9^{+2.2}_{-1.3}$
XRR080603B	2.69	238^{+51}_{-27}	$8.21^{+1.00}_{-0.79}$
XRR081221	2.26	214^{+93}_{-59}	$25.9^{+3.6}_{-2.3}$
XRR090423	8.0	439^{+66}_{-46}	$8.37^{+1.50}_{-0.85}$
XRR100615A	1.398	150^{+35}_{-17}	$5.39^{+0.84}_{-0.54}$
XRR100621A	0.542	100^{+20}_{-11}	$3.97^{+0.44}_{-0.32}$
XRR110726A	1.036	$87.2^{+23.6}_{-15.6}$	$0.148^{+0.179}_{-0.077}$
XRR120326A	1.798	114^{+16}_{-22}	$4.66^{+0.17}_{-0.17}$
XRR120802A	3.796	239^{+54}_{-33}	$3.12^{+0.18}_{-0.18}$
XRR120811C	2.671	156^{+18}_{-22}	$8.88^{+1.90}_{-1.10}$
XRR121128A	2.20	162^{+21}_{-19}	$13.0^{+1.3}_{-0.94}$
XRR130701A	1.155	191^{+180}_{-40}	$3.50^{+0.94}_{-0.45}$
XRR130925A	0.35	$48.6^{+9.8}_{-19}$	$3.11^{+0.50}_{-0.42}$
GRB080804	2.2045	523^{+120}_{-86}	$12.2^{+1.6}_{-1.3}$
GRB080916A	0.689	173^{+38}_{-25}	$1.21^{+0.10}_{-0.08}$
GRB081121	2.512	614^{+114}_{-92}	$24.4^{+3.7}_{-3.4}$
GRB081222	2.77	490^{+135}_{-124}	$27.0^{+5.1}_{-5.0}$
GRB090102	1.547	1180^{+250}_{-80}	$22.2^{+0.9}_{-0.6}$
GRB090424	0.544	237^{+34}_{-29}	$4.79^{+0.71}_{-0.79}$
GRB090926B	1.24	155^{+17}_{-15}	$4.46^{+1.82}_{-1.25}$
GRB100816A	0.8034	239^{+28}_{-25}	$0.714^{+0.209}_{-0.158}$
GRB110731A	2.83	1910^{+830}_{-570}	$44.0^{+3.0}_{-2.7}$

5. RESULTS OF THE AFTERGLOW EMISSIONS

5.1. Energy flux light-curves of X-ray afterglows

The energy-flux light curves of the X-ray afterglows in the 0.3–10 keV band of our sample observed by *Swift*/XRT are plotted in figure 7. The energy flux of the XRFs has a tendency to be slightly lower than those of the XRRs and C-GRBs. Table 4 summarizes the results of the light-curve model-fitting. Figure 8 shows $E_{\text{peak}}^{\text{obs}}$ versus energy flux at 1 hour, 10 hours, 1 day, and 10 days after the trigger time of *Swift*/BAT. These results indicate that the afterglows of the XRFs tend to be fainter than that of the C-GRBs between 10^3 – 10^4 s after the trigger time and that the tendency disappears as time elapses. We calculated the X-ray luminosity in the 0.3–10 keV band, using equation (2), for the events with known redshifts in our samples (11 XRFs, 20 XRRs, and 9 C-GRBs), and summarized the result and X-ray luminosity light-curves in tables 5 and 6 and figure 9, respectively. The above-mentioned trend in the X-ray afterglows of the XRFs is more pronounced in this figure of the energy fluxes. Furthermore, we found that if the steep decay phase ($\Gamma_1 < -2$) is ignored, the X-ray luminosities of the XRFs and XRRs decay more slowly than those of the C-GRBs.

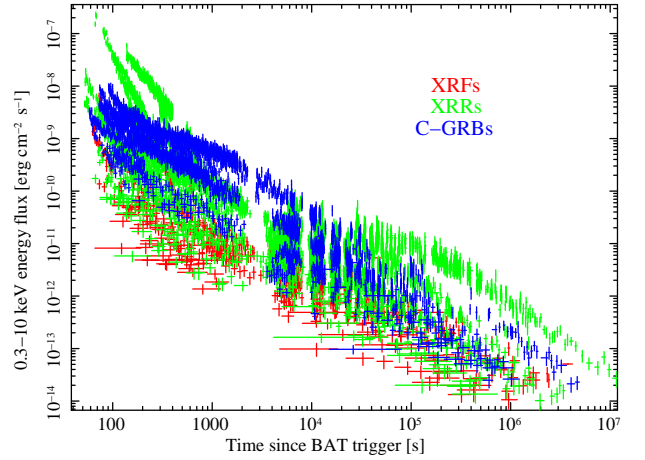


Figure 7. Energy-flux light curves of the X-Ray afterglows of all our samples.

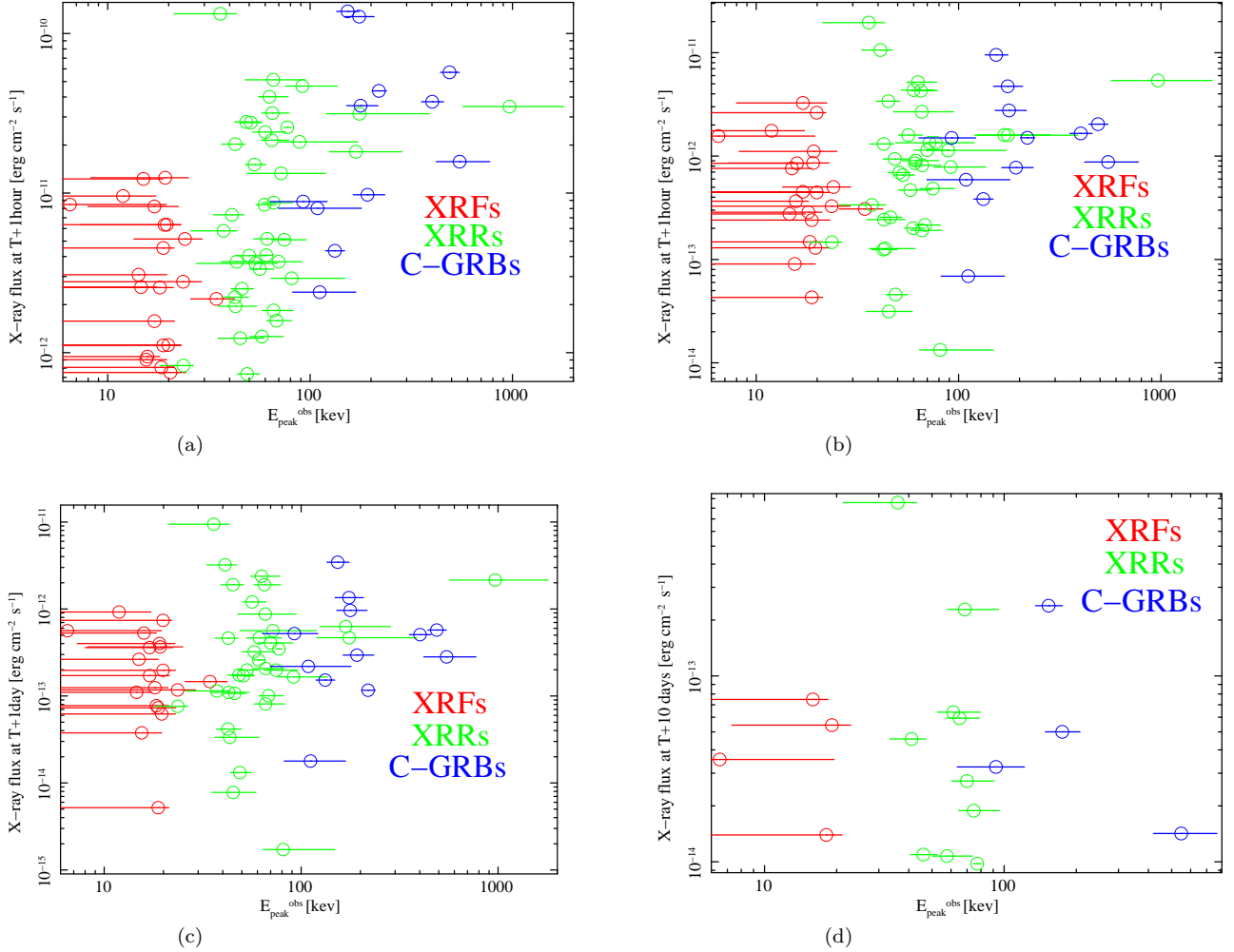


Figure 8. Energy flux at (a) 1 hour, (b) 10 hours, (c) 1 day, and (d) 10 days after the trigger time of *Swift/BAT* versus $E_{\text{peak}}^{\text{obs}}$.

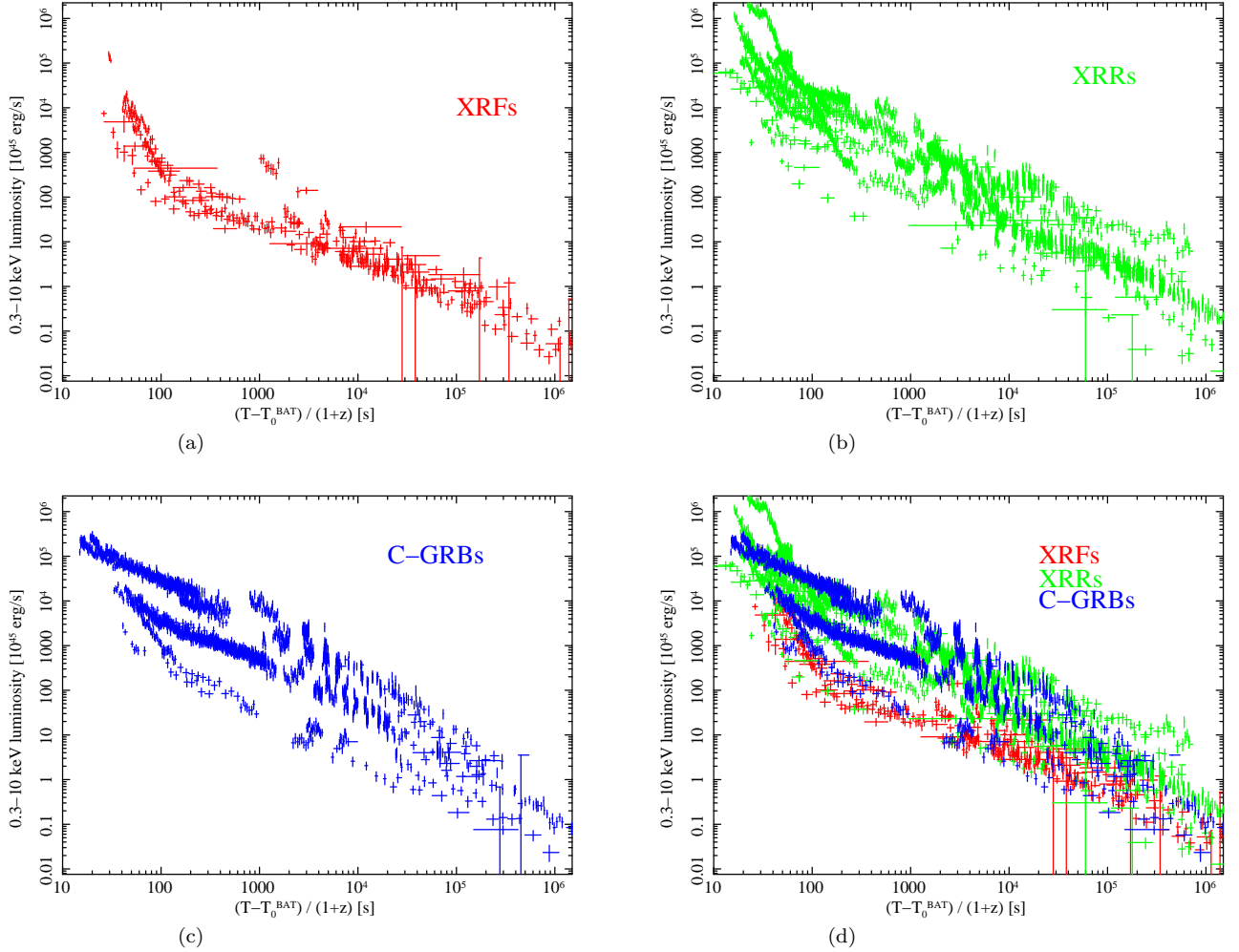


Figure 9. X-ray luminosity light-curves of (a) XRFs, (a) XRRs, (a) C-GRBs, (a) and all our samples.

Table 4. Fitting results of the X-ray afterglow light-curves (0.3–10 keV energy flux).

Events	Γ_1^a	t_1^b [sec]	Γ_2^c	t_2^d [sec]	Γ_3^e	t_3^f [sec]	Γ_4^g	$\chi^2/\text{d.o.f.}$	Best-fit model ^h
XRF050406	$-2.78^{+0.23}_{-0.20}$	917 ± 291	$-0.504^{+0.126}_{-0.128}$	1.84/5	brkpow
XRF050416A	$-1.90^{+0.32}_{-0.27}$	184 ± 5	-0.363 ± 0.021	1340^{+130}_{-110}	-0.868 ± 0.013	85.7/94	brkpow2
XRF050819	$-3.87 \pm +0.19$	441^{+26}_{-23}	$-0.738^{+0.080}_{-0.120}$	30.4/18	brkpow
XRF050824	$-0.390^{+0.069}_{-0.087}$	$6.47^{+1.50}_{-0.91} \times 10^4$	$-0.850^{+0.048}_{-0.052}$	49.0/37	brkpow
XRF060219	$-5.92^{+0.51}_{-0.57}$	222^{+8}_{-10}	-0.553 ± 0.043	$2.62^{+0.57}_{-0.59} \times 10^4$	$-1.36^{+0.10}_{-0.13}$	6.98/20	brkpow2
XRF060428B	$-4.54^{+0.12}_{-0.16}$	666^{+34}_{-40}	$-0.951^{+0.039}_{-0.048}$	133/129	brkpow
XRF060923B	$-0.612^{+0.085}_{-0.080}$	5910^{+960}_{-970}	$-2.41^{+0.34}_{-0.47}$	10.1/11	brkpow
XRF060926	$-1.45^{+0.21}_{-0.26}$	3.86/10	PL
XRF070330	-0.849 ± 0.075	17.0/17	PL
XRF070714A	$-0.537^{+0.017}_{-0.019}$	310^{+24}_{-28}	$-0.673^{+0.073}_{-0.087}$	5650^{+16000}_{-3500}	$-1.04^{+0.15}_{-0.31}$	8.47/8	brkpow2
XRF080218B	$-0.929^{+0.057}_{-0.058}$	$6.59^{+2.70}_{-1.90} \times 10^4$	$-1.72^{+0.28}_{-0.43}$	6.66/17	brkpow
XRF080520	$-1.00^{+0.08}_{-0.09}$	5.05/9	PL
XRF081007	$-4.02^{+0.13}_{-0.13}$	220 ± 5	$-0.735^{+0.016}_{-0.017}$	$3.84^{+0.88}_{-0.79} \times 10^4$	$-1.20^{+0.05}_{-0.06}$	63.9/78	brkpow2
XRF100425A	$-4.54^{+0.09}_{-0.08}$	$337^{+7.3}_{-10}$	$-0.543^{+0.029}_{-0.030}$	$4.35^{+1.20}_{-1.10} \times 10^4$	$-1.26^{+0.14}_{-0.19}$	26.9/24	brkpow2
XRF110319A	$-4.13^{+0.14}_{-0.13}$	142 ± 4	$-0.611^{+0.021}_{-0.021}$	7670^{+890}_{-850}	$-1.26^{+0.06}_{-0.07}$	64.2/64	brkpow2
XRF110808A	$-3.57^{+0.08}_{-0.09}$	564^{+23}_{-20}	$-0.400^{+0.030}_{-0.034}$	$4.35^{+1.20}_{-1.90} \times 10^4$	$-1.07^{+0.09}_{-0.11}$	28.4/30	brkpow2
XRF111129A	$-0.507^{+0.058}_{-0.055}$	3040^{+660}_{-370}	-1.21 ± 0.06	47.6/46	brkpow
XRF120116A	-2.83 ± 0.10	244 ± 11	$-0.402^{+0.033}_{-0.034}$	$3.69^{+0.31}_{-0.32} \times 10^4$	$-2.58^{+0.26}_{-0.31}$	25.1/26	brkpow2
XRF120724A	-3.95 ± 0.16	271^{+17}_{-15}	$-1.66^{+0.07}_{-0.09}$	1810^{+210}_{-160}	$-0.154^{+0.069}_{-0.082}$	9.4/17	brkpow2
XRF120816A	-1.07 ± 0.08	5700^{+1420}_{-720}	$0.056^{+0.344}_{-0.421}$	28.5/22	brkpow
XRF121108A	$-1.50^{+0.28}_{-0.19}$	658^{+284}_{-301}	$-0.845^{+0.093}_{-0.105}$	$1.64^{+1.16}_{-0.43} \times 10^4$	$-1.75^{+0.16}_{-0.22}$	20.2/22	brkpow2
XRF121212A	$-5.74^{+0.51}_{-0.44}$	936^{+28}_{-31}	-0.736 ± 0.039	48.9/43	brkpow
XRF130608A	$-4.68^{+0.24}_{-0.27}$	616^{+65}_{-54}	$-0.412^{+0.109}_{-0.102}$	30.5/30	brkpow
XRF130612A	$-0.466^{+0.099}_{-0.076}$	1280^{+1040}_{-1020}	$-1.01^{+0.06}_{-0.07}$	1.9/9	brkpow
XRF130812A	$-0.687^{+0.280}_{-0.190}$	658^{+284}_{-301}	$-0.845^{+0.093}_{-0.105}$	33.9/41	brkpow
XRF140103A	$-0.137^{+0.085}_{-0.082}$	3530^{+310}_{-280}	$-2.08^{+0.15}_{-0.21}$	42.3/35	brkpow
XRR050318	$-1.09^{+0.13}_{-0.07}$	$1.25^{+0.25}_{-0.38} \times 10^4$	$-1.92^{+0.16}_{-0.14}$	65.4/79	brkpow
XRR050410	$-1.02^{+0.05}_{-0.06}$	13.1/14	PL
XRR050525A	$-0.711^{+0.054}_{-0.049}$	7510^{+1300}_{-1600}	-1.55 ± 0.08	26.8/32	brkpow

Table 4 continued

Table 4 (*continued*)

Events	Γ_1^{a}	t_1^{b} [sec]	Γ_2^{c}	t_2^{d} [sec]	Γ_3^{e}	t_3^{f} [sec]	Γ_4^{g}	$\chi^2/\text{d.o.f.}$	Best-fit model ^h
XRR050915B	$-2.09^{+0.26}_{-0.23}$	956^{+110}_{-140}	$-0.429^{+0.030}_{-0.033}$	$8.96^{+2.10}_{-2.20} \times 10^5$	$-1.50^{+0.20}_{-0.27}$	23.3/17	brkpow2
XRR060206	$-0.925^{+0.095}_{-0.039}$	1700^{+820}_{-650}	$-0.429^{+0.031}_{-0.027}$	$2.78^{+0.21}_{-0.38} \times 10^4$	$-1.18^{+0.09}_{-0.08}$	26.4/28	brkpow2
XRR060707	$-1.75^{+0.13}_{-0.12}$	419 ± 110	$-0.758^{+0.029}_{-0.033}$	$7.15^{+4.80}_{-2.40} \times 10^5$	$-2.01^{+0.46}_{-0.48}$	36.7/44	brkpow2
XRR060825	$-0.983^{+0.048}_{-0.045}$	10.5/11	PL
XRR060927	$-0.758^{+0.17}_{-0.070}$	4370^{+1600}_{-2000}	$-1.53^{+0.21}_{-0.41}$	8.71/15	brkpow
XRR061222B	$-3.34^{+0.15}_{-0.14}$	415^{+34}_{-49}	$-1.59^{+0.01}_{-0.13}$	36.4/38	brkpow
XRR070612B	$-2.34^{+0.018}_{-0.022}$	10.3/6	PL
XRR070721A	$-2.80^{+0.31}_{-0.51}$	325^{+49}_{-40}	$-0.752^{+0.057}_{-0.057}$	4.77/16	brkpow
XRR071010B	$-0.663^{+0.064}_{-0.063}$	7.09/16	PL
XRR080207	0.190 ± 0.230	342^{+58}_{-45}	$-1.78^{+0.06}_{-0.07}$	139/144	brkpow
XRR080212	$-8.01^{+0.08}_{-0.07}$	594^{+3}_{-4}	$-0.282^{+0.019}_{-0.022}$	5890^{+390}_{-370}	-1.13 ± 0.05	$2.34^{+0.56}_{-0.36} \times 10^4$	$-1.56^{+0.10}_{-0.12}$	198/198	brkpow3
XRR080603B	$-3.45^{+0.16}_{-0.22}$	151^{+8}_{-9}	$-0.835^{+0.035}_{-0.041}$	100/96	brkpow
XRR081128	$-4.89^{+0.14}_{-0.15}$	473^{+32}_{-26}	$-0.992^{+0.043}_{-0.046}$	44.0/47	brkpow
XRR081221	$-5.81^{+0.08}_{-0.07}$	205 ± 1	$-0.707^{+0.029}_{-0.025}$	717^{+40}_{-41}	-1.28 ± 0.01	$3.54^{+0.74}_{-1.40} \times 10^5$	$-3.12^{+1.60}_{-0.44}$	433/383	brkpow3
XRR090423	$-5.79^{+0.27}_{-0.23}$	341^{+4}_{-3}	$0.001^{+0.390}_{-0.100}$	5100^{+260}_{-260}	$-1.42^{+0.07}_{-0.08}$	35.2/47	brkpow2
XRR090429B	$0.81^{+0.39}_{-0.26}$	657^{+140}_{-88}	$-1.25^{+0.06}_{-0.07}$	17.5/20	brkpow
XRR090531A	$-0.673^{+0.87}_{-0.91}$	2.31/4	PL
XRR090813	$-0.237^{+0.080}_{-0.067}$	445^{+42}_{-37}	-1.15 ± 0.02	9340^{+3000}_{-3100}	-1.40 ± 0.07	314/297	brkpow2
XRR090912	$-0.744^{+0.037}_{-0.037}$	55.2/57	PL
XRR100615A	$-4.23^{+0.31}_{-0.45}$	192 ± 2	$-0.084^{+0.036}_{-0.036}$	2840^{+180}_{-170}	-0.889 ± 0.035	89.1/90	brkpow2
XRR100621A	$-3.80^{+0.027}_{-0.024}$	419^{+5}_{-4}	$-0.626^{+0.013}_{-0.014}$	5790^{+720}_{-520}	-0.932 ± 0.018	$1.13^{+0.12}_{-0.16} \times 10^5$	$-1.58^{+0.14}_{-0.14}$	416/354	brkpow3
XRR101022A	$-0.372^{+0.622}_{-0.652}$	0.55/3	PL
XRR101024A	$-1.38^{+0.47}_{-0.36}$	$121^{+4.7}_{-3.9}$	$0.032^{+0.06}_{-0.06}$	1010^{+38}_{-47}	$-1.36^{+0.066}_{-0.073}$	50.0/55	brkpow2
XRR110411A	$-5.79^{+0.38}_{-0.52}$	$244^{+4.2}_{-4.1}$	$-0.473^{+0.039}_{-0.040}$	3560^{+930}_{-650}	$-1.24^{+0.069}_{-0.081}$	53.1/48	brkpow2
XRR110726A	$-0.853^{+0.052}_{-0.051}$	16.7/11	PL
XRR120102A	$-3.82^{+0.38}_{-0.32}$	163 ± 8	-0.570 ± 0.026	$1.13^{+0.06}_{-0.09} \times 10^4$	$-1.05^{+0.02}_{-0.03}$	$1.74^{+0.34}_{-0.39} \times 10^5$	$-1.47^{+0.23}_{-0.34}$	155.4/154	brkpow3
XRR120326A	-3.09 ± 0.03	402 ± 6	-0.139 ± 0.013	$1.14^{+0.08}_{-0.07} \times 10^4$	$0.464^{+0.036}_{-0.034}$	$4.32^{+0.12}_{-0.07} \times 10^4$	$-1.85^{+0.07}_{-0.06}$	209.6/233	brkpow3
XRR120703A	$-2.45^{+0.30}_{-0.28}$	125 ± 8	$-0.621^{+0.029}_{-0.028}$	3880^{+400}_{-380}	-1.07 ± 0.02	$3.42^{+0.56}_{-0.38} \times 10^5$	$-4.29^{+1.39}_{-3.08}$	95.0/80	brkpow3
XRR120802A	$-2.79^{+0.28}_{-0.41}$	257^{+39}_{-40}	$-0.372^{+0.059}_{-0.055}$	29.0/31	brkpow
XRR120811C	$-3.20^{+0.12}_{-0.15}$	225 ± 10	$-0.474^{+0.054}_{-0.057}$	2820^{+840}_{-530}	-1.19 ± 0.07	140/106	brkpow2
XRR120927A	$-3.33^{+0.02}_{-0.01}$	185^{+13}_{-15}	$-0.885^{+0.040}_{-0.039}$	9770^{+1570}_{-1150}	$-2.19^{+0.28}_{-0.37}$	25.0/28	brkpow2

Table 4 continued

Table 4 (continued)

KATSUKURA ET AL.

Events	Γ_1^a	t_1^b [sec]	Γ_2^c	t_2^d [sec]	Γ_3^e	t_3^f [sec]	Γ_4^g	$\chi^2/\text{d.o.f.}$	Best-fit model ^h
XRR121123A	$-5.39^{+0.08}_{-0.04}$	1360^{+10}_{-20}	$-0.320^{+0.023}_{-0.020}$	$1.63^{+0.07}_{-0.10} \times 10^4$	$-1.36^{+0.08}_{-0.06}$	210.0/185	brkpow2
XRR121128A	$-4.18^{+0.33}_{-0.16}$	149^{+2}_{-3}	$-0.548^{+0.038}_{-0.022}$	1500 ± 90	$-1.60^{+0.04}_{-0.03}$	110.0/105	brkpow2
XRR130627A	$-0.873^{+0.125}_{-0.139}$	14.0/17	PL
XRR130701A	$-2.24^{+0.19}_{-0.18}$	123 ± 4	$-0.785^{+0.043}_{-0.048}$	471^{+53}_{-48}	-1.27 ± 0.02	110.0/123	brkpow2
XRR130727A	$-0.994^{+0.046}_{-0.051}$	43.0/46	PL
XRR130925A	-2.43 ± -0.02	903^{+11}_{-12}	-0.832 ± 0.004	$3.11^{+0.25}_{-0.19} \times 10^5$	$-1.30^{+0.02}_{-0.03}$	900/799	brkpow2
XRR140108A	$-3.06^{+0.13}_{-0.11}$	405 ± 7	-0.497 ± 0.015	7070^{+330}_{-260}	$-1.31^{+0.03}_{-0.02}$	340/225	brkpow2
GRB080714	-1.13 ± 0.03	71.5/43	PL
GRB080804	$-1.10^{+0.01}_{-0.02}$	82.3/101	PL
GRB080916A	$-3.41^{+0.14}_{-0.14}$	319^{+33}_{-28}	$-0.745^{+0.074}_{-0.071}$	$3.17^{+1.50}_{-1.20} \times 10^4$	$-1.21^{+0.08}_{-0.09}$	97.0/117	brkpow2
GRB081121	-1.43 ± 0.02	193/147	PL
GRB081222	$-0.888^{+0.024}_{-0.024}$	635^{+120}_{-110}	$-1.11^{+0.02}_{-0.02}$	$7.82^{+1.70}_{-2.60} \times 10^4$	$-1.97^{+0.24}_{-0.24}$	492/418	brkpow2
GRB090102	$-0.977^{+0.171}_{-0.160}$	1460^{+990}_{-590}	-1.45 ± 0.04	139/139	brkpow
GRB090424	$-0.874^{+0.065}_{-0.070}$	1540^{+140}_{-200}	$-1.16^{+0.03}_{-0.01}$	$5.92^{+5.75}_{-3.90} \times 10^5$	$-1.42^{+0.20}_{-0.22}$	691/663	brkpow2
GRB090926B	$-2.25^{+0.10}_{-0.12}$	660^{+130}_{-100}	-1.01 ± 0.12	82.8/99	brkpow
GRB100816A	$-2.64^{+0.80}_{-0.79}$	150^{+45}_{-26}	-1.05 ± 0.04	43.3/38	brkpow
GRB110610A	$-2.91^{+0.28}_{-0.22}$	194^{+27}_{-29}	$-0.130^{+0.749}_{-0.348}$	930^{+579}_{-197}	$-1.16^{+0.06}_{-0.08}$	43.0/50	brkpow2
GRB110625A	$-2.67^{+0.56}_{-0.70}$	166^{+8}_{-10}	-1.12 ± 0.04	$2.32^{+0.43}_{-0.41} \times 10^4$	$-2.92^{+0.45}_{-0.77}$	53.0/49	brkpow2
GRB110731A	$-2.83^{+0.35}_{-0.67}$	94^{+4}_{-3}	-1.15 ± 0.02	7100^{+4690}_{-2160}	$-1.30^{+0.06}_{-0.05}$	310/301	brkpow2
GRB121011A	$-1.54^{+0.03}_{-0.04}$	24.0/19	PL
GRB131229A	-1.01 ± 0.05	424^{+277}_{-144}	$-1.35^{+0.04}_{-0.06}$	210/226	brkpow

^aDecay index of the 1st power-law component.^bBreak time of the 1st component in seconds after the BAT trigger.^cDecay index of the 2nd power-law component.^dBreak time of the 2nd component in seconds after the BAT trigger.^eDecay index of the 3rd power-law component.^fBreak time of the 3rd component in seconds after the BAT trigger.^gDecay index of the 4th power-law component.^hThe models “brkpow”, “brkpow2”, and “brkpow3” have two, three, and four decay indices of power-law components, respectively.

5.2. X-ray luminosity and the temporal index at 200 seconds after the BAT trigger

Figure 10 shows the plots of X-ray luminosity versus $E_{\text{peak}}^{\text{src}}$, temporal decay index versus $E_{\text{peak}}^{\text{src}}$, X-ray luminosity versus E_{iso} , and temporal decay index versus E_{iso} . The X-ray luminosity and the temporal decay index are derived at 200 seconds after the *Swift*/BAT trigger time in the rest frame of the GRBs. The number of the samples is 38. The correlation coefficients σ for the four plots are $\sigma = 0.33 \pm 0.08$, $-0.38^{+0.03}_{-0.06}$, $0.54^{+0.07}_{-0.06}$, and -0.47 ± 0.02 , respectively. Therefore, $E_{\text{peak}}^{\text{src}}$ and E_{iso} , both of which were derived from the spectrum of the prompt emission, are moderately correlated with the X-ray luminosity and the temporal decay index in the afterglow emission. In consequence, we confirmed that X-ray afterglow luminosity of the GRBs with a lower $E_{\text{peak}}^{\text{src}}$, i.e., softer GRBs, tend to be dimmer and to decay more slowly than harder GRBs. Note that we had excluded

the data of XRR050318 and XRR071010B because we could not estimate their luminosity at the epoch due to lack of the BAT data.

5.3. X-ray luminosity and the temporal index at 10 hours after the BAT trigger

Figure 11 shows the same four plots as of figure 10 but for the epoch 10 hours after the *Swift*/BAT trigger time. The number of the samples is 39. The correlation coefficients are $\sigma = 0.10^{+0.08}_{-0.07}$, $-0.09^{+0.05}_{-0.04}$, $0.08^{+0.06}_{-0.08}$, and $-0.27^{+0.05}_{-0.03}$, respectively, for the four plots. In contrast to those at the epoch 200s after the trigger (the previous subsection), no clear correlations among those properties were found. Note that we had excluded the data of XRF120724A because of lack of the data (the available XRT data covered up to only 2.7 hours after the BAT trigger).

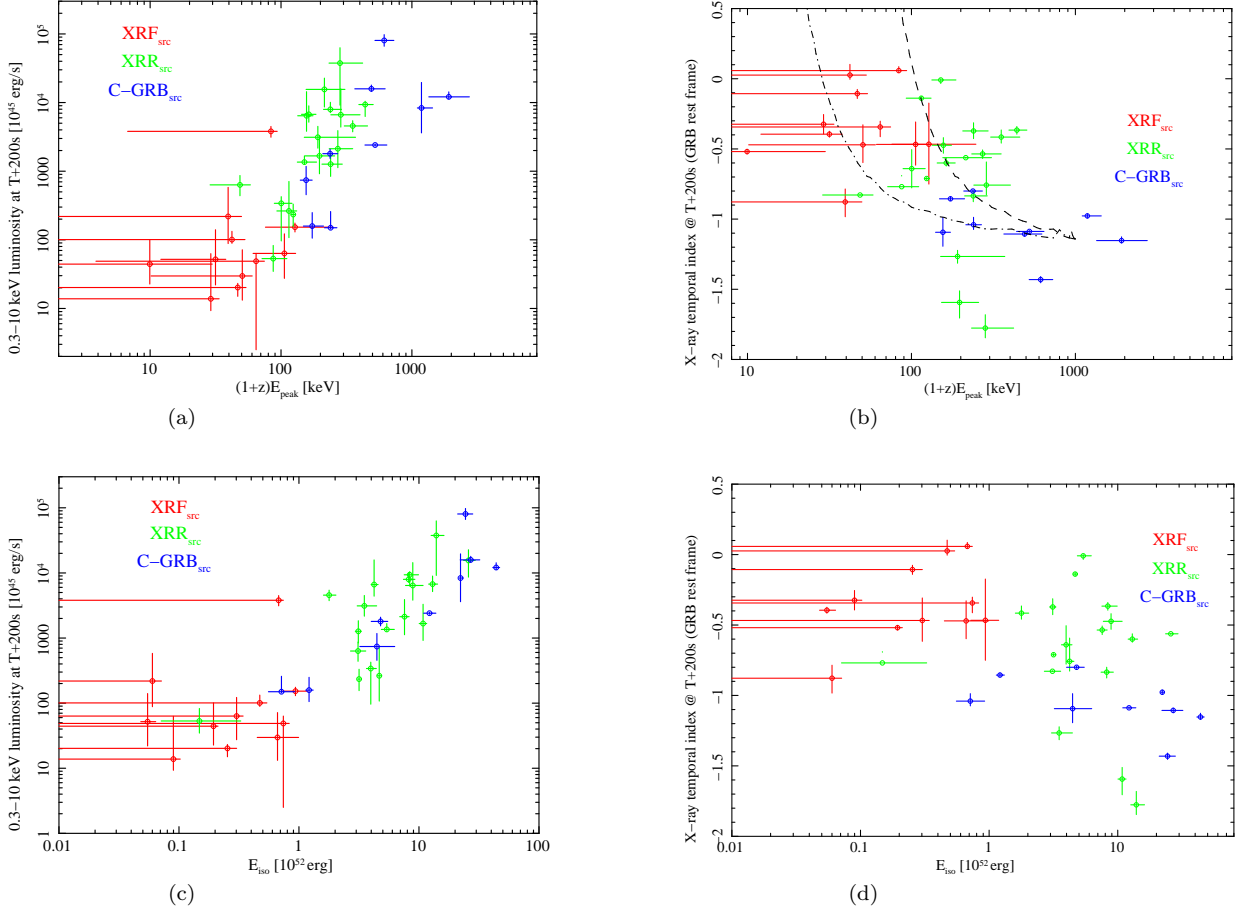


Figure 10. Relations between the prompt emission and early afterglow. (a) X-ray luminosity versus $E_{\text{peak}}^{\text{src}}$. (b) Temporal decay index versus $E_{\text{peak}}^{\text{src}}$. The dashed and dot-dashed lines are the indices derived from the boxfit light-curves with the assumed Γ of 100 and 1000, respectively, and $(1+z)E_{\text{peak}}^{\text{on}} = 1000$ keV, where θ_{obs} is allowed to vary for an range of 0–0.01 rad ($\approx 0.6^\circ$). (c) X-ray luminosity versus E_{iso} . (d) Temporal decay index versus E_{iso} . These afterglow parameters are derived 200 seconds after the *Swift/BAT* trigger time in the rest frame of the GRBs.

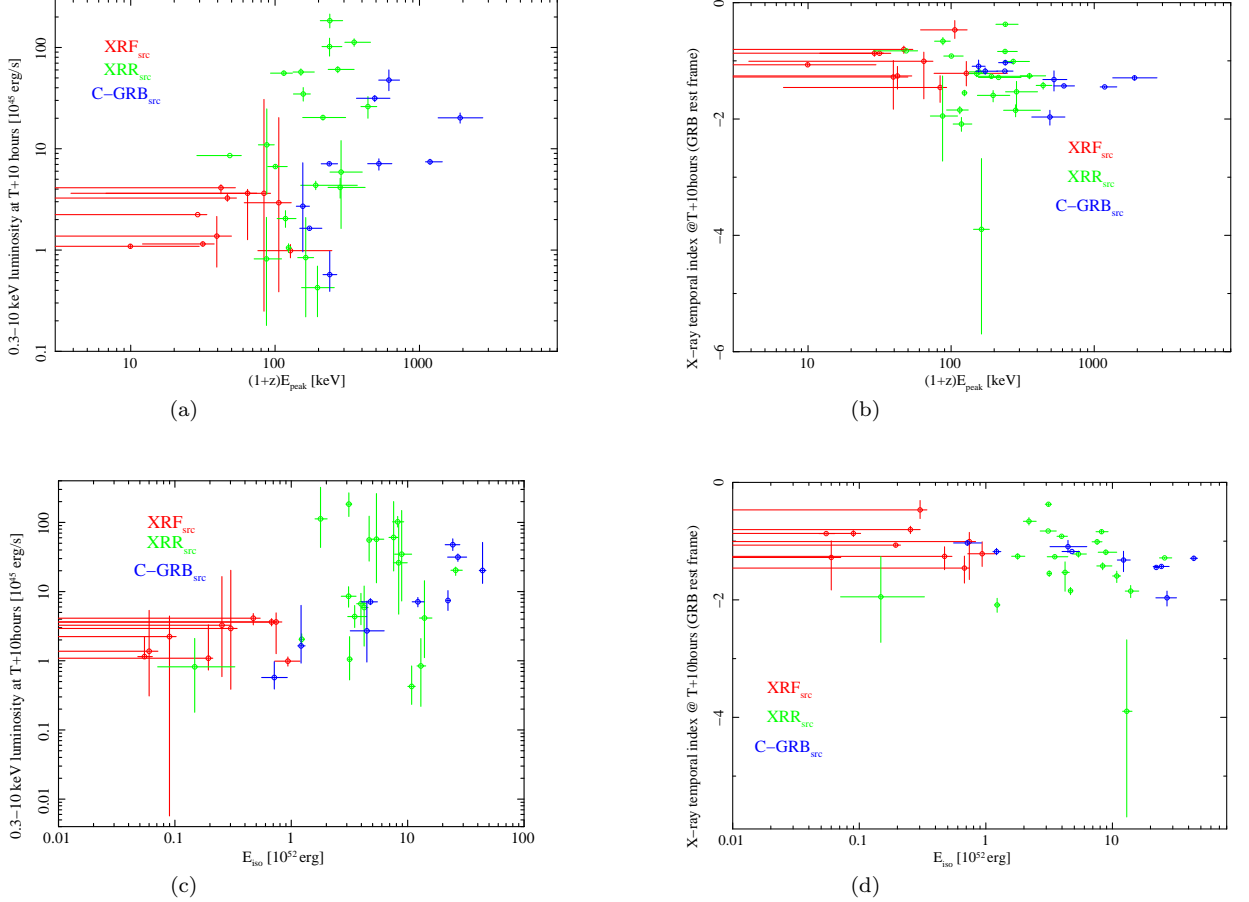


Figure 11. Same as figure 10 but for the parameters of the afterglow 36000 seconds after the *Swift/BAT* trigger time.

Table 5. Fitting results of the X-ray afterglow light-curves (0.3–10 keV luminosity).

Events	Γ_1^{a}	t_1^{b} [sec]	Γ_2^{c}	t_2^{d} [sec]	Γ_3^{e}	t_3^{f} [sec]	Γ_4^{g}	$\chi^2/\text{d.o.f.}$	Best-fit model ^h
XRF050406	$-0.468^{+0.160}_{-0.148}$	$63.3^{+59.0}_{-35.9}$	$-0.395^{+0.022}_{-0.021}$	891^{+81}_{-85}	$-0.871^{+0.012}_{-0.014}$	86.1/94	brkpow2
XRF050416A	-1.55 ± 0.01	122 ± 4	$-0.395^{+0.022}_{-0.021}$	891^{+81}_{-85}	$-0.871^{+0.012}_{-0.014}$	86.1/94	brkpow2
XRF050819	-3.25 ± 0.02	270^{+51}_{-58}	$-0.344^{+0.049}_{-0.055}$	8660^{+5600}_{-2740}	$-1.04^{+0.18}_{-0.64}$	30.4/16	brkpow2
XRF050824	$-0.324^{+0.006}_{-0.007}$	$3.53^{+0.59}_{-0.49} \times 10^4$	$-0.869^{+0.047}_{-0.054}$	48.6/37	brkpow
XRF060926	$-1.66^{+0.024}_{-0.027}$	$37.8^{+2.2}_{-1.6}$	$0.056^{+0.029}_{-0.015}$	300^{+20}_{-26}	$-1.46^{+0.06}_{-0.07}$	6.37/11	brkpow2
XRF080520	$-1.53^{+0.44}_{-0.33}$	157^{+84}_{-78}	$-0.877^{+0.092}_{-0.11}$	5140^{+17000}_{-3200}	$-1.28^{+0.28}_{-0.55}$	1.96/3	brkpow2
XRF081007	-3.73 ± 0.01	179^{+11}_{-6}	$-0.533^{+0.03}_{-0.003}$	5630^{+630}_{-670}	$-1.07^{+0.03}_{-0.02}$	84.3/73	brkpow2
XRF100425A	$-4.65^{+0.01}_{-0.02}$	141^{+3}_{-2}	$0.026^{+0.077}_{-0.082}$	421^{+56}_{-54}	$-0.651^{+0.029}_{-0.032}$	$2.12^{+0.58}_{-0.61} \times 10^4$	$-1.26^{+0.16}_{-0.23}$	17.8/21	brkpow3
XRF110808A	-3.57 ± 0.01	293^{+10}_{-9}	$-0.106^{+0.037}_{-0.041}$	5820^{+1100}_{-1000}	$-0.804^{+0.058}_{-0.068}$	$(1.29 \pm 0.31) \times 10^5$	$-2.04^{+0.67}_{-1.0}$	26.4/28	brkpow3
XRF120724A	$-0.471^{+0.143}_{-0.127}$	$29.7^{+41.8}_{-16.5}$	$0.005^{+0.020}_{-0.021}$	3560^{+130}_{-140}	$-2.84^{+0.23}_{-0.27}$	56.8/34	brkpow2
XRF130612A	$-0.467^{+0.293}_{-0.284}$	152 ± 23	$0.005^{+0.020}_{-0.021}$	3560^{+130}_{-140}	$-2.84^{+0.23}_{-0.27}$	56.8/34	brkpow2
XRR050318	-1.23 ± 0.01	7330^{+670}_{-700}	$-2.09^{+0.11}_{-0.13}$	68.4/75	brkpow
XRR050525A	-0.711 ± 0.008	4680^{+450}_{-450}	-1.55 ± 0.05	26.8/28	brkpow
XRR060206	$-0.925^{+0.014}_{-0.015}$	320^{+52}_{-47}	-0.416 ± 0.031	5920^{+620}_{-640}	$-1.26^{+0.04}_{-0.05}$	12.7/20	brkpow2
XRR060707	-2.80 ± 0.01	112 ± 3	$-0.535^{+0.022}_{-0.024}$	7050^{+1700}_{-1500}	$-1.01^{+0.04}_{-0.05}$	$2.46^{+0.50}_{-0.36} \times 10^5$	$-2.35^{+0.49}_{-0.69}$	46.6/38	brkpow3
XRR060927	$-0.757^{+0.017}_{-0.018}$	662^{+130}_{-110}	$-1.53^{+0.18}_{-0.32}$	8.71/14	brkpow
XRR061222B	-3.35 ± 0.01	$95.2^{+6.1}_{-6.6}$	$-1.59^{+0.08}_{-0.11}$	36.3/38	brkpow
XRR071010B	$-0.663^{+0.064}_{-0.063}$	8.71/14	PL
XRR080207	-1.69 ± 0.01	4080^{+1900}_{-1400}	$-1.85^{+0.095}_{-0.11}$	44.1/60	brkpow
XRR080603B	$-3.50^{+0.01}_{-0.01}$	$40.4^{+1.0}_{-0.8}$	$-0.839^{+0.028}_{-0.032}$	100/92	brkpow
XRR081221	-0.562 ± 0.004	209 ± 8	-1.28 ± 0.01	$9.16^{+4.31}_{-2.49} \times 10^4$	$-2.32^{+0.83}_{-1.30}$	255/262	brkpow2
XRR090423	-4.88 ± 0.02	$38.7^{+0.8}_{-0.7}$	$-0.366^{+0.026}_{-0.028}$	1340^{+190}_{-180}	$-1.48^{+0.08}_{-0.12}$	17.5/17	brkpow2
XRR100615A	-4.22 ± 0.01	81.5 ± 0.8	-0.009 ± 0.026	454^{+45}_{-39}	$-0.480^{+0.021}_{-0.021}$	8590^{+870}_{-840}	$-1.22^{+0.05}_{-0.05}$	70.7/87	brkpow3
XRR100621A	-3.77 ± 0.01	$274^{+2.5}_{-2.3}$	$-0.640^{+0.011}_{-0.012}$	4050^{+370}_{-440}	$-0.918^{+0.018}_{-0.017}$	$5.72^{+0.95}_{-0.50} \times 10^4$	$-1.52^{+0.05}_{-0.06}$	416/356	brkpow3
XRR110726A	$-0.853^{+0.052}_{-0.051}$	16.7/11	PL
XRR120326A	$-4.54^{+0.0062}_{-0.0058}$	$93.1^{+0.56}_{-0.56}$	$-0.136^{+0.0072}_{-0.0068}$	4490^{+160}_{-270}	$0.469^{+0.025}_{-0.029}$	$(1.56 \pm 0.03) \times 10^4$	$-1.84^{+0.06}_{-0.07}$	176/194	brkpow3
XRR120802A	-2.79 ± 0.02	$53.5^{+1.8}_{-1.6}$	$-0.372^{+0.023}_{-0.025}$	28.9/31	brkpow
XRR120811C	-3.22 ± 0.01	$60.0^{+1.3}_{-1.1}$	$-0.504^{+0.028}_{-0.029}$	808 ± 98	-1.19 ± 0.04	140/106	brkpow2
XRR121128A	-4.90 ± 0.01	$43.4^{+0.4}_{-0.3}$	$-0.600^{+0.020}_{-0.021}$	466^{+28}_{-32}	$-1.55^{+0.04}_{-0.03}$	$1.70^{+0.25}_{-0.24} \times 10^4$	$-3.90^{+1.21}_{-1.80}$	117/119	brkpow3

Table 5 continued

Table 5 (continued)

Events	Γ_1^a	t_1^b [sec]	Γ_2^c	t_2^d [sec]	Γ_3^e	t_3^f [sec]	Γ_4^g	$\chi^2/\text{d.o.f.}$	Best-fit model ^h
XRR130701A	-2.07 ± 0.01	$61.8^{+1.4}_{-1.3}$	-0.703 ± 0.040	195^{+17}_{-18}	-1.27 ± 0.02	119/124	brkpow2
XRR130925A	-2.43 ± 0.02	903^{+11}_{-12}	-0.832 ± 0.004	$3.11^{+0.25}_{-0.19} \times 10^5$	$-1.30^{+0.02}_{-0.03}$	900/799	brkpow2
GRB080804	-1.09 ± 0.01	$1.71^{+2.10}_{-0.87} \times 10^4$	$-1.32^{+0.15}_{-0.20}$	77.1/99	brkpow
GRB080916A	-3.31 ± 0.01	172 ± 3	$-0.856^{+0.016}_{-0.013}$	$2.42^{+0.78}_{-0.51} \times 10^4$	$-1.18^{+0.06}_{-0.05}$	175/130	brkpow2
GRB081121	-1.43 ± 0.02	193/145	PL
GRB081222	-2.14 ± 0.01	20.9 ± 0.2	-0.837 ± 0.001	148^{+11}_{-10}	-1.11 ± 0.01	$2.08^{+0.30}_{-0.29} \times 10^4$	$-1.97^{+0.12}_{-0.14}$	455/416	brkpow3
GRB090102	-0.977 ± 0.005	575^{+51}_{-48}	$-1.45^{+0.01}_{-0.02}$	139/138	brkpow
GRB090424	-2.20 ± 0.01	97.9 ± 1.0	$-0.800^{+0.009}_{-0.008}$	920^{+53}_{-62}	-1.18 ± 0.01	542/663	brkpow2
GRB090926B	$-2.27^{+0.11}_{-0.13}$	290^{+54}_{-44}	$-1.09^{+0.11}_{-0.13}$	75.4/88	brkpow
GRB100816A	-1.03 ± 0.04	24.2/27	PL
GRB110731A	-1.16 ± 0.01	1860^{+1200}_{-600}	-1.29 ± 0.04	261/249	brkpow

^aDecay index of the 1st power-law component.

^bBreak time of the 1st component in seconds after the BAT trigger.

^cDecay index of the 2nd power-law component.

^dBreak time of the 2nd component in seconds after the BAT trigger.

^eDecay index of the 3rd power-law component.

^fBreak time of the 3rd component in seconds after the BAT trigger.

^gDecay index of the 4th power-law component.

^hBest-fit model. The models “brkpow”, “brkpow2”, and “brkpow3” have two, three, and four decay indices of power-law components, respectively.

Table 6. X-ray luminosity and temporal decay index 200, 3600, and 36000 sec after the BAT trigger time in the rest frame of the GRBs.

Events	L_{200}^{a}	Γ_{200}^{b}	L_{3600}^{c}	Γ_{3600}^{d}	L_{36000}^{e}	$\Gamma_{36000}^{\text{f}}$
XRF050406	$63.3^{+59.0}_{-35.9}$	$-0.468^{+0.160}_{-0.148}$	$8.61^{+33.00}_{-7.53}$	$-0.468^{+0.160}_{-0.148}$	$2.93^{+17.40}_{-2.55}$	$-0.468^{+0.160}_{-0.148}$
XRF050416A	52.0^{+88}_{-29}	-0.395 ± 0.021	$8.54^{+7.40}_{-6.69}$	$-0.871^{+0.012}_{-0.014}$	$1.15^{+1.1}_{-0.6}$	$-0.871^{+0.012}_{-0.014}$
XRF050819	48.8^{+14}_{-46}	$-0.344^{+0.042}_{-0.069}$	$18.1^{+2.9}_{-2.9}$	$-0.344^{+0.048}_{-0.056}$	$3.64^{+1.30}_{-2.40}$	$-1.01^{+0.16}_{-0.65}$
XRF050824	$13.8^{+49}_{-4.5}$	$-0.324^{+0.069}_{-0.069}$	$4.77^{+19.00}_{-1.10}$	$-0.324^{+0.007}_{-0.006}$	$2.24^{+2.20}_{-2.20}$	$-0.869^{+0.047}_{-0.054}$
XRF060926	3800^{+680}_{-680}	$0.056^{+0.029}_{-0.015}$	104^{+12}_{-12}	$-1.46^{+0.20}_{-0.26}$	3.63 ± 0.44	$-1.46^{+0.20}_{-0.26}$
XRF080520	218^{+360}_{-130}	$-0.877^{+0.09}_{-0.110}$	$17.3^{+39.0}_{-13.0}$	$-0.877^{+0.092}_{-0.110}$	$1.37^{+4.00}_{-1.10}$	$-1.28^{+0.28}_{-0.55}$
XRF081007	$44.3^{+56.0}_{-21.0}$	$-0.519^{+0.017}_{-0.018}$	$9.88^{+6.30}_{-5.60}$	$-0.533^{+0.032}_{-0.003}$	$1.09^{+2.20}_{-0.35}$	$-1.07^{+0.03}_{-0.02}$
XRF100425A	100^{+32}_{-11}	$0.026^{+0.077}_{-0.030}$	25.4^{+64}_{-18}	$-0.651^{+0.029}_{-0.032}$	$4.12^{+0.69}_{-0.82}$	$-1.26^{+0.16}_{-0.23}$
XRF110808A	$20.2^{+3.0}_{-5.2}$	$-0.106^{+0.030}_{-0.034}$	$14.8^{+27.0}_{-3.2}$	$-0.106^{+0.037}_{-0.041}$	$3.26^{+3.00}_{-2.7}$	$-0.804^{+0.058}_{-0.068}$
XRF120724A	$29.7^{+41.8}_{-16.5}$	$-0.471^{+0.143}_{-0.127}$	$7.62^{+20.1}_{-5.27}$	$-0.155^{+0.068}_{-0.080}$
XRF130612A	153 ± 23	$-0.467^{+0.293}_{-0.284}$	16.2 ± 2.4	$-1.22^{+0.20}_{-0.22}$	0.986 ± 0.148	$-1.22^{+0.20}_{-0.22}$
XRR050318	135^{+48}_{-38}	-1.23 ± 0.04	$2.05^{+0.40}_{-0.37}$	$-2.09^{+0.11}_{-0.13}$
XRR050525A	234^{+97}_{-78}	-0.711 ± 0.008	$30.0^{+12.2}_{-10.1}$	$-0.711^{+0.0076}_{-0.0081}$	$1.05^{+1.2}_{-0.52}$	-1.55 ± 0.053
XRR060206	4560^{+870}_{-810}	$-0.416^{+0.051}_{-0.043}$	1340^{+100}_{-530}	-0.416 ± 0.031	112^{+210}_{-69}	$-1.26^{+0.04}_{-0.05}$
XRR060707	2130^{+1800}_{-1000}	$-0.535^{+0.029}_{-0.033}$	452^{+380}_{-210}	$-0.535^{+0.022}_{-0.024}$	60.7^{+140}_{-40}	$-1.01^{+0.04}_{-0.05}$
XRR060927	6630^{+9200}_{-2200}	$-0.758^{+0.170}_{-0.070}$	200^{+70}_{-83}	$-1.53^{+0.18}_{-0.32}$	$5.88^{+6.22}_{-4.20}$	$-1.53^{+0.18}_{-0.32}$
XRR061222B	1670^{+1600}_{-750}	$-1.59^{+0.08}_{-0.11}$	$16.7^{+16.0}_{-7.5}$	$-1.59^{+0.08}_{-0.11}$	$0.426^{+0.412}_{-0.191}$	$-1.59^{+0.08}_{-0.11}$
XRR071010B	$50.3^{+54.1}_{-31.2}$	$-0.663^{+0.064}_{-0.063}$	$10.9^{+13.8}_{-7.4}$	$-0.663^{+0.064}_{-0.063}$
XRR080207	37600^{+25000}_{-28000}	$-1.78^{+0.10}_{-0.07}$	287^{+460}_{-190}	-1.69 ± 0.006	$4.15^{+10.25}_{-3.00}$	$-1.85^{+0.1-}_{-0.11}$
XRR080603B	7960^{+2100}_{-830}	-0.835 ± 0.041	704^{+140}_{-110}	-0.839 ± 0.03	102^{+20}_{-16}	$-0.839^{+0.028}_{-0.032}$
XRR081221	15600^{+7100}_{-6900}	-0.562 ± 0.004	392^{+43}_{-61}	-1.28 ± 0.01	$20.3^{+2.3}_{-3.2}$	-1.28 ± 0.01
XRR090423	9360^{+1100}_{-3100}	$-0.366^{+0.026}_{-0.029}$	690^{+1400}_{-490}	-1.42 ± 0.06	$26.1^{+67.0}_{-21.1}$	-1.42 ± 0.06
XRR100615A	1360^{+310}_{-90}	$-0.00871^{+0.00831}_{-0.02690}$	498^{+590}_{-270}	-0.480 ± 0.0210	$57.2^{+200.5}_{-43.2}$	-1.22 ± 0.05
XRR100621A	340^{+85}_{-240}	-0.640 ± 0.140	$53.4^{+13.2}_{-38.0}$	$-0.640^{+0.011}_{-0.012}$	$6.67^{+2.80}_{-3.40}$	$-0.918^{+0.018}_{-0.017}$
XRR110726A	$63.3^{+38.0}_{-27.4}$	$-0.853^{+0.052}_{-0.051}$	$5.38^{+3.96}_{-2.67}$	$-0.853^{+0.052}_{-0.051}$	$0.755^{+0.670}_{-0.417}$	$-0.853^{+0.052}_{-0.051}$
XRR120326A	263^{+450}_{-160}	$-0.139^{+0.012}_{-0.013}$	149^{+320}_{-110}	-0.136 ± -0.007	$55.8^{+67.0}_{-28.0}$	$-1.84^{+0.059}_{-0.067}$
XRR120802A	1270^{+570}_{-430}	$-0.372^{+0.058}_{-0.055}$	432^{+200}_{-150}	$-0.372^{+0.023}_{-0.025}$	183^{+83}_{-62}	$-0.372^{+0.023}_{-0.025}$
XRR120811C	6420^{+8000}_{-2600}	$-0.474^{+0.054}_{-0.057}$	537^{+1100}_{-380}	-1.19 ± 0.04	$34.7^{+110.0}_{-27.0}$	-1.19 ± 0.043

Table 6 continued

Table 6 (*continued*)

Events	L_{200}^{a}	Γ_{200}^{b}	L_{3600}^{c}	Γ_{3600}^{d}	L_{36000}^{e}	$\Gamma_{36000}^{\text{f}}$
XRR121128A	6740^{+2200}_{-1600}	$-0.600^{+0.038}_{-0.022}$	171^{+70}_{-62}	$-1.55^{+0.03}_{-0.04}$	$0.842^{+1.211}_{-0.620}$	$-3.90^{+1.22}_{-1.80}$
XRR130701A	3120^{+1400}_{-960}	$-1.27^{+0.04}_{-0.05}$	$80.4^{+35.0}_{-24.0}$	-1.27 ± 0.02	$4.36^{+1.92}_{-1.31}$	-1.27 ± 0.02
XRR130925A	631^{+240}_{-190}	-0.828 ± 0.004	$57.6^{+21.2}_{-17.3}$	$-0.828^{+0.0037}_{-0.0035}$	$8.56^{+3.20}_{-2.60}$	-0.828 ± 0.004
GRB080804	2410^{+88}_{-89}	-1.09 ± 0.01	103^{+12}_{-11}	-1.09 ± 0.01	7.12 ± 1.1	$-1.32^{+0.15}_{-0.20}$
GRB080916A	158^{+90}_{-52}	$-0.856^{+0.016}_{-0.013}$	$13.4^{+9.3}_{-3.8}$	$-0.856^{+0.016}_{-0.013}$	$1.64^{+4.71}_{-0.71}$	$-1.18^{+0.06}_{-0.05}$
GRB081121	80400^{+17000}_{-14000}	-1.43 ± 0.02	1290^{+280}_{-230}	-1.43 ± 0.02	$47.6^{+10.0}_{-8.4}$	-1.43 ± 0.02
GRB081222	15900^{+2100}_{-1400}	-1.11 ± 0.02	645^{+81}_{-59}	-1.11 ± 0.01	$31.5^{+3.5}_{-4.2}$	$-1.97^{+0.12}_{-0.14}$
GRB090102	8340^{+11000}_{-4700}	$-0.977^{+0.017}_{-0.016}$	208^{+81}_{-58}	$-1.45^{+0.01}_{-0.02}$	$7.43^{+2.90}_{-2.10}$	$-1.45^{+0.01}_{-0.02}$
GRB090424	1800^{+290}_{-260}	-0.800 ± 0.01	106^{+12}_{-10}	-1.18 ± 0.01	$7.10^{+0.83}_{-0.64}$	-1.18 ± 0.01
GRB090926B	740^{+435}_{-286}	$-1.09^{+0.11}_{-0.10}$	$33.6^{+40.5}_{-19.6}$	$-1.09^{+0.11}_{-0.10}$	$2.71^{+4.56}_{-1.75}$	$-1.09^{+0.11}_{-0.10}$
GRB100816A	149^{+110}_{-6}	$-1.04^{+0.05}_{-0.03}$	$6.14^{+3.60}_{-1.80}$	-1.03 ± 0.04	$0.572^{+0.400}_{-0.180}$	-1.03 ± 0.04
GRB110731A	12100^{+2200}_{-800}	$-1.15^{+0.03}_{-0.02}$	395^{+610}_{-140}	-1.29 ± 0.041	$20.2^{+31.1}_{-7.1}$	-1.29 ± 0.04

^a0.3–10 keV luminosity (10^{45} erg s $^{-1}$) 200 s after the BAT trigger time.

^bDecay index in the afterglow light-curve of 0.3–10 keV luminosity 200 sec after the BAT trigger time.

^c0.3–10 keV luminosity (10^{45} erg s $^{-1}$) 3600 s after the BAT trigger time.

^dDecay index in the afterglow light-curve of 0.3–10 keV luminosity 3600 sec after the BAT trigger time.

^e0.3–10 keV luminosity (10^{45} erg s $^{-1}$) 36000 s after the BAT trigger time.

^fDecay index in the afterglow light-curve of 0.3–10 keV luminosity 36000 sec after the BAT trigger time.

6. DISCUSSION

6.1. Comparison of the observed afterglow light-curves with the boxfit simulation

We used the “boxfit” (van Eerten et al. 2012) tool to perform simulations of the afterglows for their light curves in order to verify whether the origin of the E_{peak} diversity in prompt emission is the properties of jet or the geometrical effect.

6.1.1. The variable opening angle jet model

The variable opening angle jet model is one of the model which explains the E_{peak} diversity by the properties of jet itself. Figure 12 shows the simulated light curves of the X-ray afterglow with the tools on the basis of the variable opening-angle model, where the jet opening angles $\Delta\theta$ are allowed to vary. In the simulations, we have used the values of E_{iso} calculated from following equation given by Lamb et al. (2005),

$$E_{\text{iso}} = \frac{E_{\gamma}}{1 - \cos \Delta\theta}, \quad (3)$$

where E_{γ} is the energy of emitted photon energy and we assumed it $E_{\gamma} = 1.3 \times 10^{51}$, estimated by Bloom et al. (2003). The events with a larger $\Delta\theta$ (or lower E_{iso}) are found to have a lower X-ray luminosity than those with a smaller $\Delta\theta$ (higher E_{iso}). Also, figure 12 implies that the break time of the jets with a smaller $\Delta\theta$ comes earlier. The positive correlation between the X-ray luminosity and E_{iso} (or “hardness” of the events) exists only in the early phase of afterglows and disappears in the later phase. Accordingly, the simulated X-ray luminosity light-curves on the basis of the variable opening-angle model are consistent with the observed $L_{\text{X}}-E_{\text{peak}}^{\text{src}}$ (E_{iso}) relations.

The range of E_{iso} in our sample, however, is $10^{50} < E_{\text{iso}} < 10^{54}$ erg, and the lower limit is 10 times smaller than E_{γ} estimated by Bloom et al. (2003). Thus, there is no value of the opening angle that can accommodate this value of E_{iso} . According to Lamb et al. (2005), in order to escape this problem, E_{γ} is rescaled and the equation 3 is modified to be

$$E_{\text{iso}} = \frac{E_{\gamma}}{95 \times (1 - \cos \Delta\theta)}. \quad (4)$$

In the basis of this equation, we obtained the range of $\Delta\theta$, corresponding to that of E_{iso} . The range is $5.2 \times 10^{-3} < \Delta\theta < 0.53$ rad.

Here, we estimate range of jet break time (t_{jet}) from those of $\Delta\theta$ and of E_{iso} . t_{jet} means the break time in the light curve of the afterglow. After the t_{jet} , the temporal decay index become smaller than -2 (Sari et al. 1999).

The t_{jet} is given by the equation (1) in Sari et al. (1999),

$$t_{\text{jet}} \approx 6.2(E_{\text{iso},52}/n)^{1/3}(\Delta\theta/0.1)^{8/3}, \quad (5)$$

where $E_{\text{iso},52}$ is the isotropic equivalent energy in units of 10^{52} ergs. If we assume circum-burst number density $n = 1$ [cm^{-3}], the range of t_{jet} is $40 < t_{\text{jet}} < 4 \times 10^5$ sec. Therefore, It is necessary that jet breaks are occurred in afterglow light curves of energetic GRBs ($E_{\text{iso}} > 2.0 \times 10^{54}$ erg) before 200 sec after trigger. The results shown in §5.1, however, are inconsistent with the prediction of such a early jet break.

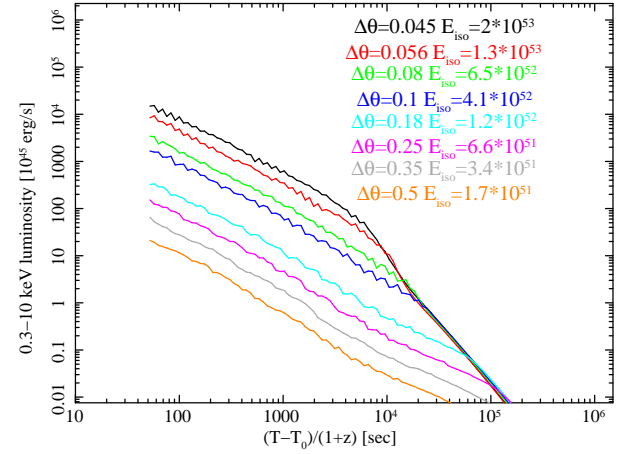


Figure 12. Light curves simulated with the boxfit tools on the basis of the variable opening-angle model, where the jet opening angle $\Delta\theta$ and E_{iso} are allowed to vary. The fixed parameters are $\theta_{\text{obs}} = 0$, $n = 1$, $p = 2.5$, $\epsilon_B = 10^{-5}$, and $\epsilon_e = 0.2$.

6.1.2. The off-axis jet model

Another likely model of GRBs is the off-axis model, in which the situation of an observer being off-axis from the jet is considered. The off-axis model predicts an existence of a rising part in the afterglow light curve because its beamed emission is less visible to the observer in the early phase. Figure 13 shows the X-ray luminosity light-curves simulated with the boxfit tools on the basis of the off-axis model. The results suggest the trend that the peak of light curves and start time of the rising part come later for the events with a wider θ_{obs} . The trend is consistent with the results from our observed samples (see §5.1), which have indicated that the X-ray luminosity of the XRF samples are lower than those of C-GRBs. However, our observation results (figures 8–10) do not show any significant rising parts as in figure 13(a). Therefore, these results suggest that the diversity in the observing angles has to be restricted in a very narrow range of $\theta_{\text{obs}} < 0.01$ rad ($\approx 0.6^\circ$) on the basis of the off-axis model.

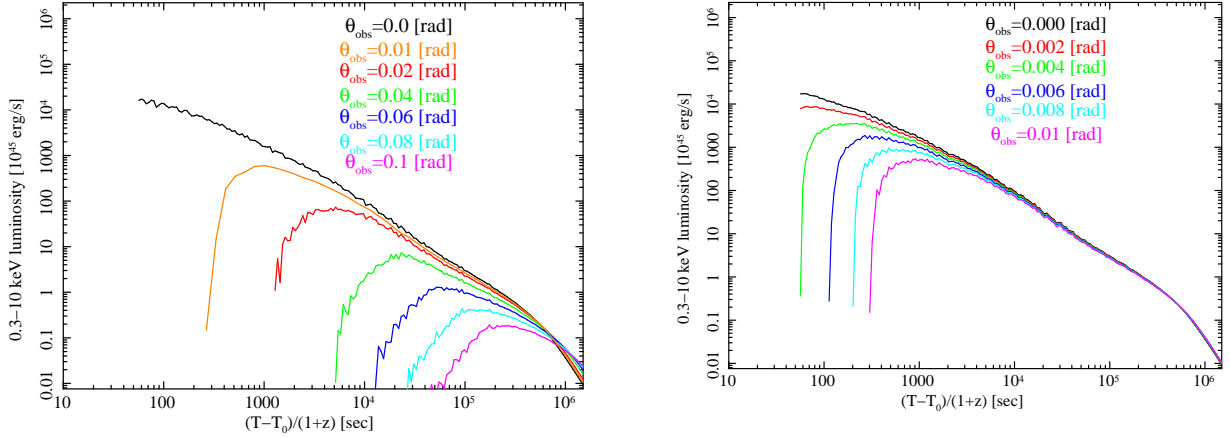


Figure 13. Simulated light curves with the boxfit tools on the basis of the off-axis model with the varying observing angle θ_{obs} for a range of (left) 0–0.1 rad ($\approx 6^\circ$), drawn every 0.02 rad, (right) 0–0.01 rad ($\approx 0.6^\circ$), drawn every 0.002 rad. See figure 12 caption for the fixed parameters.

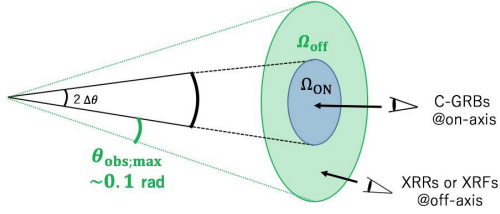


Figure 14. Assumed geometry of the GRB jet in §6. We assume that C-GRBs are observed in the on-axis (blue) area, whereas XRFs and XRRs are observed in the off-axis (green) area. The parameter Ω_{ON} (Ω_{OFF}) is the solid angle subtended by the direction to which a source is observed as a C-GRB (XRR or XRF), and $\theta_{\text{obs},\text{max}}$ is the observing angle at which hard GRBs ($E_{\text{peak}}^{\text{obs}} = 100 \text{ keV}$) are observed as XRFs ($E_{\text{peak}}^{\text{obs}} = 1$).

6.2. Total number of XRFs, XRRs, and C-GRBs in the whole universe

To restrict the viable theoretical models, we estimate the total numbers of the XRFs, XRRs, and C-GRBs in the whole universe per year, using the simulator publicly available by Graff et al. (2016), based on the *Swift/BAT* trigger algorithm (Lien et al. 2014; Graff et al. 2016). We execute the simulator setting the maximum likelihood parameters as given in (Graff et al. 2016) (the result of the random forest, figure 15). In consequence, we obtain the total numbers of C-GRBs $f_{\text{C-GRB}} = 570 \pm 36$ [events yr⁻¹], XRRs $f_{\text{XRR}} = 3031 \pm 53$ [events yr⁻¹], and XRFs $f_{\text{XRF}} = 968 \pm 45$ [events yr⁻¹], where the errors are determined from the Gaussian distribution obtained after running the simulator 10000 times.

Here, the intrinsic local GRB event rate which we used is $n_0 = 0.42$ [events Gpc⁻³ yr⁻¹], derived in (Graff et al. 2016). This rate is consistent with the rate of “high-luminosity GRBs”, corresponding to C-

GRBs and XRRs, of ~ 0.45 [events Gpc⁻³ yr⁻¹]. In contrast, the rate of sub-energetic GRBs (GRB980425 and GRB060218) of 230^{+490}_{-190} [events Gpc⁻³ yr⁻¹] (Soderberg et al. 2006) and the rate of 10.6 [events Gpc⁻³ yr⁻¹] as measured by *HETE-2* (Pélaud et al. 2008) are ~ 1000 and ~ 25 times higher, respectively, than the rate which we used for the estimation. Especially in the latter one, the population of gamma-ray bursts is dominated by the X-ray flashes. Thus, the estimated total number of the XRFs is a lower limit because the previous studies suggest that the total number of the XRFs was underestimated.

Next, we calculate the canonical opening angle $\Delta\theta$ and bulk Lorentz factor Γ of the jets from the obtained total numbers. We assume that the on-axis GRBs are observed as C-GRBs in an area of Ω_{on} and off-axis ones as XRRs or XRFs in an area of Ω_{off} , as illustrated in figure 14. Their ratio is given by, according to Yamazaki et al. (2002),

$$\frac{\Omega_{\text{off}}}{\Omega_{\text{on}}} = \frac{2\pi[1 - \cos(\theta_{\text{obs},\text{max}} + \Delta\theta)] - 2\pi[1 - \cos(\Delta\theta)]}{2\pi[1 - \cos(\Delta\theta)]}, \quad (6)$$

where $\theta_{\text{obs},\text{max}}$ is the observing angle at which E_{peak} is observed as 1 keV due to the relativistic Doppler effect. We consider that the C-GRBs, XRRs, and XRFs have $E_{\text{peak}}^{\text{obs}} > 100 \text{ keV}$, $100 \geq E_{\text{peak}}^{\text{obs}} > 30 \text{ keV}$, and $30 \geq E_{\text{peak}}^{\text{obs}} \geq 1 \text{ keV}$, respectively, on the basis of the results of §4.1. According to §4 in Yamazaki et al. (2002), the quantity $f_{\text{XRF}} + f_{\text{XRR}}$ ($f_{\text{C-GRB}}$) is the solid angle subtended by the direction to which the source is observed as an XRF or XRR (C-GRB). Thus, the ratio of the solid angles of an off-axis to on-axis observers can be described as the ratio of the numbers of the off-axis

to on-axis events,

$$\frac{\Omega_{\text{off}}}{\Omega_{\text{on}}} = \frac{f_{\text{XRR}} + f_{\text{XRF}}}{f_{\text{C-GRB}}} \gtrsim 7. \quad (7)$$

We substitute $\theta_{\text{obs;max}} \sim 0.01$, which is estimated in §6.1.2, into equation (6), solve it for $\Delta\theta$, and find that

$$\Delta\theta \lesssim 5.5 \times 10^{-3} [\text{rad}] \approx 0.32^\circ. \quad (8)$$

The $f_{\text{C-GRB}}$ is identified with the total number of the jets pointed to the Earth per year, which are launched from the sources in the whole universe, such as core-collapse supernovae. Thus, $f_{\text{src}} = f_{\text{C-GRB}}/\Omega_{\text{on}} \approx 6.1 \times 10^6$ is corresponding to the total number of the jets which are launched from the source in the whole universe per year.

Here, we estimate jet break time (t_{jet}) of XRF from the $\Delta\theta$, using equation 5. If we assume circum-burst number density $n = 1 [\text{cm}^{-3}]$ and the energy of the jet as $E_{\text{iso}} = 4.4 \times 10^{53} [\text{erg}]^2$, the jet break time is $t_{\text{jet}} \lesssim 30$ sec. However, none of XRFs in our sample showed the significant feature of jet break (see in §5.1).

The relation between E_{peak} of an on-axis ($E_{\text{peak}}^{\text{on}}$) and off-axis ($E_{\text{peak}}^{\text{off}}$) observers is given by (Yamazaki et al. 2002),

$$E_{\text{peak}}^{\text{off}} = \frac{\delta(1 - \beta)}{\Gamma} E_{\text{peak}}^{\text{on}} = \frac{1 - \beta}{1 - \beta \cos(\theta_{\text{obs}})} E_{\text{peak}}^{\text{on}} \quad (9)$$

where β is the velocity of the jet and δ is the Doppler factor. Substituting $E_{\text{peak}}^{\text{off}} = 1 \text{ keV}$, $E_{\text{peak}}^{\text{on}} = 100 \text{ keV}$, and $\theta_{\text{obs}} = \theta_{\text{obs;max}} \sim 0.01$ into equation 9, we find the bulk Lorentz factor $\Gamma \approx 1000$.

If we assume to be $E_{\text{peak}}^{\text{off}} = 10 \text{ keV}$, the total number of the XRFs and the ratio of solid angle decrease to $f_{\text{XRF};E_{\text{peak}}>10\text{keV}} = 539 \pm 36$ [events yr^{-1}] and $\Omega_{\text{off}}/\Omega_{\text{on}} \gtrsim 6$, respectively. The values of $\Delta\theta$, t_{jet} , and Γ , corresponding to be based on this condition are $\Delta\theta \lesssim 5.9 \times 10^{-3} [\text{rad}] \approx 0.34^\circ$, $t_{\text{jet}} \lesssim 40 \text{ s}$, and $\Gamma \approx 300$. This Γ is smaller than the value derived in the basis of the assumption to be $E_{\text{peak}}^{\text{off}} = 1 \text{ keV}$. On the other hand, the results that $\Delta\theta$ is narrow and t_{jet} is too fast, are same as the former one.

In summary, a XRF is observed when a narrow ($\Delta\theta \sim 0.3^\circ$) jet is viewed at $\theta_{\text{obs}} \sim 0.6^\circ$. Thus, the E_{peak} diversity, which is apparent in the BAT samples, needs to be explained despite a very small variation in the jet viewing angle, $0 < \theta_{\text{obs}} \lesssim 0.6^\circ$, of the XRFs. This result supports the conclusion by Donaghy (2006), in which the mechanism generating the $E_{\text{peak}}^{\text{src}} - E_{\text{iso}}$ relation (Amati et al. 2002) was discussed. Additionally,

the t_{jet} corresponding to estimated $\Delta\theta$ is 30s (or 40s) and none of XRFs in our sample showed the significant feature of jet break. Therefore, the E_{peak} diversity among GRBs observed by *Swift*/BAT, *Fermi*/GBM and others are likely to mainly originate not from the off-axis effect but rather the properties of the jet itself, e.g., the variable opening angles.

6.3. Multi-band light curve fitting with the boxfit tools.

In order to not only constrain values of $\Delta\theta$ and θ_{obs} more strongly than the estimations from the event rates but also to find out whether the optical and X-ray afterglow are the same component of external shock models (as expected in the standard model e.g., Frail et al. (2000)), we executed a model fit for the boxfit-simulated data for the X-ray and optical afterglows originally observed by *Swift*/XRT and optical telescopes on the ground, respectively. Table 7 summarizes the samples used. Those samples were selected from our analyzed samples whose optical data were rich.

For the data of the C-GRBs, we used the parameter region of E_{iso} derived from our analysis of the prompt emissions. For the other data, while the lower limit of E_{iso} was set the same as those for the C-GRBs, we did not set the upper limit because the simulated jet energy E_j in the boxfit tools relates to E_{iso} by

$$E_j = E_{\text{iso}}(1 - \cos \Delta\theta) \approx E_{\text{iso}} \Delta\theta^2 / 2, \quad (10)$$

and because we have to consider the attenuation of E_{iso} caused by off-axis effects in order not to underestimate the jet energy.

Table 8 summarizes the fitting results of the 5 samples that we used. We found the negative correlation between E_{iso} (or $E_{\text{peak}}^{\text{src}}$) and the opening angle of the jet, i.e., the sources with a smaller E_{iso} (or $E_{\text{peak}}^{\text{src}}$) have a larger opening angle. The observing angles of all the sample sources were 0° . These imply that these XRRs and XRFs are the on-axis events. Figure 15 shows the multi-band light-curves of the samples. XRR050525A and XRR090423 showed the consistent fits to the X-ray and optical data. However, the other three samples showed unacceptable fits, especially with the X-ray data.

This result implies that an origin of X-ray afterglow emissions different from that of optical one. The observed data of our samples are rather inconsistent with the predicted afterglow light-curve on the basis of the external shock model.

Although our discussion has been based on the assumption that both the X-ray and optical emissions originate in the external shock, the possibility that the emissions actually come from some different processes is not

² This value is the maximum in our sample (GRB110731A).

Table 7. Samples used for the boxfit simulations.

Events	Energy band or filters
XRF050416A	X-ray ^a , R ^b , K _s ^c
XRF081007	X-ray ^a , r',H ^d
XRR050525A	X-ray ^a , V,UVW1 ^e
XRR090423	X-ray ^a , J,K,H ^f
GRB090102	X-ray ^a , r',z ^g

^a[Evans et al. \(2009\)](#). We used the monochromatic flux at the 0.3 keV and 10 keV bands.

^b[Soderberg et al. \(2007\)](#)

^c[Kann et al. \(2010\)](#)

^d[Jinet al. \(2013\)](#)

^e[Blustin et al. \(2006\)](#)

^f[Tanvir et al. \(2009\)](#)

^g[Gemire et al. \(2010\)](#)

els, the off-axis jet model, which proposes that the off-axis viewing angle of an observer to the jet plays an important role in the observed properties of the XRFs.

7.2. Suggestions from box-fit results

We executed a model fit for the boxfit-simulated data for the X-ray and optical afterglows in 2 XRFs, 2 XRRs, and 1 C-GRBs, respectively. This fitting results shows that the observing angles of all the sample sources were 0°, and this suggested that the XRRs and the XRFs are on-axis events. On the other hand, simulated multi-band light-curves in the samples showed unacceptable fits, especially with the X-ray data. The results implied that the external shock model alone could not explain the X-ray afterglows.

This work is supported by MEXT KAKENHI Grant Numbers 17H06357 and 17H06362. The authors would like to thank R. Yamazaki for useful discussion. We also thank Y. Kawakubo, K. Senuma, and H. Ohtsuki for technical assistance with our analysis. Finally, we are grateful to the referees for useful comments.

totally excluded. Discussion about the possibility is out of scope of this paper.

7. CONCLUSIONS

7.1. Conclusions about off-axis model

We performed a systematic study of GRBs observed by *Swift* by investigating the prompt and afterglow emissions. We cataloged the long GRBs observed by the *Swift* between 2004 December and 2014 February, classifying them into three categories of XRFs, XRRs, and C-GRBs, according to the classification method of [Sakamoto et al. \(2008\)](#). We analyzed the spectra of these sources during the t_{100} interval in the prompt emission and derived $E_{\text{peak}}^{\text{obs}}$, and also calculated $E_{\text{peak}}^{\text{src}}$ for those with known redshifts. Analyzing X-ray afterglows of the GRB samples with well-constrained E_{peak} , we confirmed that $E_{\text{peak}}^{\text{src}}$ and E_{iso} are moderately correlated with the X-ray luminosity and the temporal decay index. Furthermore, we estimated total numbers of the XRFs, XRRs, and C-GRBs in the whole universe per year, to be $f_{\text{C-GRB}} = 570 \pm 36$, $f_{\text{XRR}} = 3031 \pm 53$, and $f_{\text{XRF}} = 968 \pm 45$ ($f_{\text{XRF}; E_{\text{peak}} > 10 \text{ keV}} = 539 \pm 36$) [events yr⁻¹], respectively. With these event rates, the canonical opening angle $\Delta\theta$ and bulk Lorentz factor Γ of the jets of the XRFs were estimated to be $\Delta\theta \lesssim 0.3^\circ$ (corresponding to $\theta_{\text{obs}} \sim 0.6^\circ$), $t_{\text{jet}} \lesssim 30 \text{ s} (\lesssim 40 \text{ s})$ and $\Gamma \approx 1000$, respectively. We thus conclude that the observer requires to be close to the jet on-axis for the XRFs. This rejects one of the popular theoretical mod-

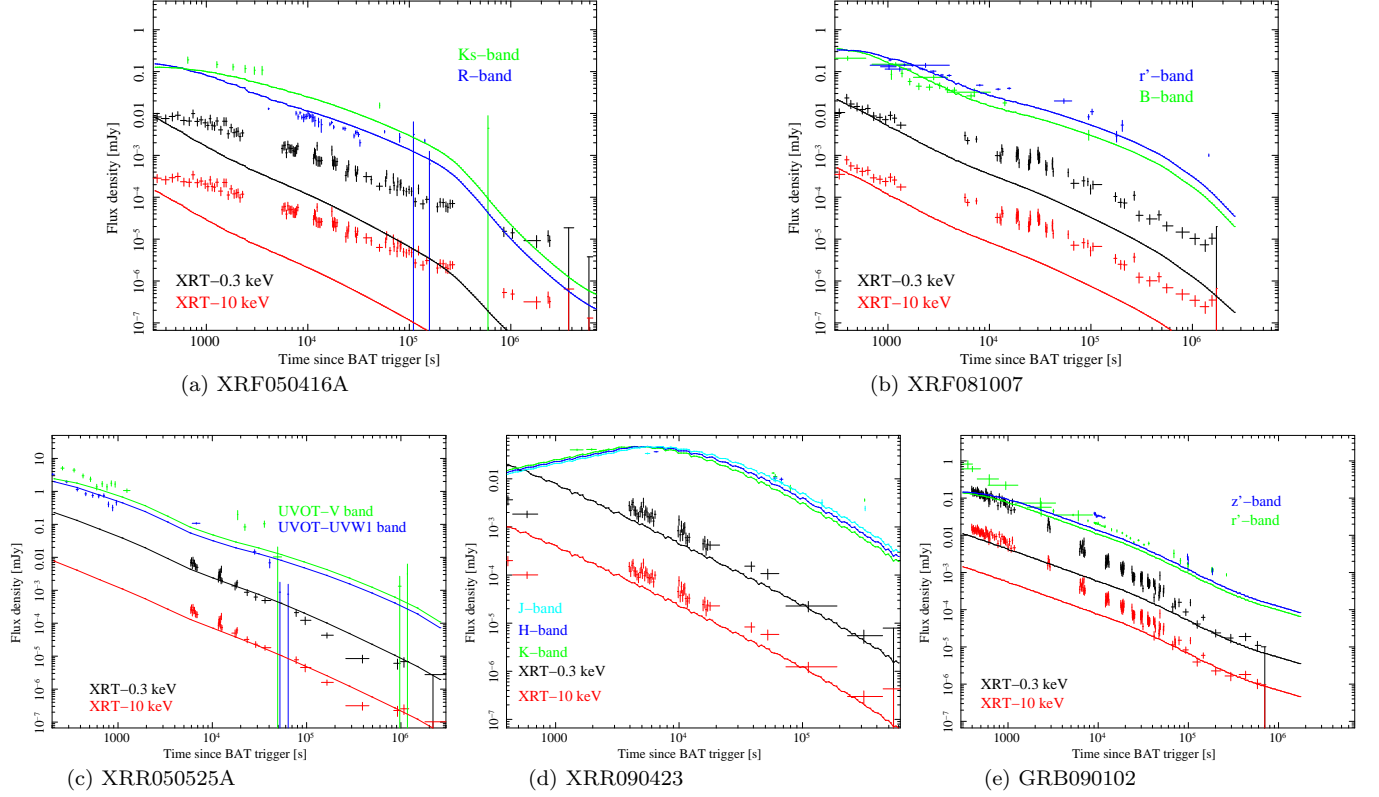


Figure 15. Multi-band light curves: (a) XRF050416A, (b) XRF081007, (c) XRR050525A, (d) XRR090423, and (e) GRB090102. The data points are the observed light curves and solid lines are simulated light curves with the boxfit tools (See table 8).

Table 8. Parameters derived by model fitting with the boxfit tools. The fraction (ϵ_e) of the downstream internal energy in the shock-accelerated electrons is fixed at $\epsilon_e = 0.2$ for all the samples. The observing angle of the C-GRB (GRB090102) is fixed at $\theta_{obs} = 0$.

Events	$\Delta\theta^h$ [rad]	θ_{obs}^i [rad]	E_{iso} [10^{52} erg]	n^j [cm^{-3}]	p^k	ϵ_B^l [10^{-5}]	χ^2/dof
XRF050416A	0.4949	0	0.05208	2.147	2.177	906.9	12.76
XRF081007	0.4136	0	0.0957	10.19	2.136	274.2	11.93
XRR050525A	0.3817	0	1.608	34.38	2.100	14.91	19.61
XRR090423	0.05788	0	159.5	0.1331	2.697	0.8967	10.11
GRB090102	0.1909	0 (fixed)	150.5	0.3802	2.164	0.0618	11.25

^hJet half-opening angle

ⁱObserving angle

^jCircum-burst number density

^kSynchrotron slope

^lThe fraction of downstream internal energy in the shock-generated magnetic field

REFERENCES

- Amati, L., et al. 2002, A&A, 390, 81
- Amati, L., 2006, MNRAS, 372, 233
- Band, D. L. 1993, ApJ, 413, 281
- Barraud, C., et al. 2005, A&A, 400, 1021
- Barraud, C., Daigne, F., Mochkovitch, R., & Atteia, J. L. 2005, A&A, 440, 809
- Barthelmy, S. D., et al. 2005, SSRv, 120, 143
- Berger, E. 2014, ARA&A, 54, 43
- Bloom, J. S. et al. 1999, Nature, 401, 453
- Bloom, J., Frail, D. A., Kulkarni, S. R. 2003, ApJ, 588, 945
- Blustin, A. J. et al. 2006, ApJ, 637, 901
- Burrows, S. D., et al. 2005a, SSRv, 120, 165
- Burrows, S. D., et al. 2005b, Science, 309, 1833B
- Dermer, C. D., et al. 1999, ApJ, 513, 656
- Donaghy, T. Q. 2006, ApJ, 645, 436
- Evans, P. A., Beardmore, A. P., Page, K. L., et al. 2009, MNRAS, 397, 1177
- Frail, D. A., Waxman, E., & Kulkarni, S. R. 2000, ApJ, 537, 191
- Frail, D. A., et al. 2001, ApJ, 562, L55
- Gehrels, N., et al. 2004, ApJ, 611, 1005
- Gemire, B., et al. 2010, MNRAS, 405, 2372
- Graff, P. B., Lien, A., et al. 2016, ApJ, 818, 55
- Gruber, D., et al. 2014, ApJS, 211, 12
- Heise, J. 2003, in AIP Conf. Proc. 662, Gamma-Ray Burst and Afterglow Astronomy 2001: A Workshop Celebrating the First Year of the HETE Mission, ed. G. R. Ricker & R. K. Vanderspek (Melville, NY: AIP), 229
- Heise, J., Zand, J. I., Kippen, R. M., & Woods, P. M. 2001, in Gamma-ray Bursts in the Afterglow Era, ed. E. Costa, F. Frontera, & J. Hjorth (Berlin: Springer), 16
- Jin, Zhi-Ping, et al. 2013, ApJ, 774, 114
- Kaneko, Y., et al. 2006, ApJS, 166, 29
- Kann, D. A., et al. 2010, ApJ, 720, 1513
- Kippen, R. M., Woods, P. M., Heise, J., int Zand, J. J. M., Briggs, M. S., & Preece, R. D. 2003, in AIP Conf. Proc. 662, Gamma-Ray Burst and Afterglow Astronomy 2001, ed. G. R. Ricker & R. K. Vanderspek (New York: AIP), 244
- Kiziloglu, U., et al. 2006, GRB Coordinates Network, Circular Service, No. 5618, #1
- Kornilov, V., et al. 2006, GRB Coordinates Network, Circular Service, No. 5901, #1
- Lamb, D. Q., et al. 2005, ApJ, 620, 355
- Lien, A., Fields, B. D. 2009, JCAP, 1, 47
- Lien, A., Sakamoto, T., Gehrels, N., et al. 2014, ApJ, 783, 24
- Lien, A., Sakamoto T., Barthelmy, S. D., et al. 2016, ApJ, 829, 7
- Meegan, C. A., et al. 1996, ApJS, 106, 65
- Meegan, C., Lichti, G., Bhat, P. N., et al. 2009, ApJ, 702, 791
- Paciesas, W. S., et al. 1999, ApJS, 122, 465
- Racusin, J. L., Karpov, S. V., Sokolowski, M., et al. 2008, Nature, 455, 183
- Racusin, J. L., et al. 2016, ApJ, 826, 45
- Pélagneon, A., Atteia, J.-L., Nakagawa, Y. E., et al. 2008, A&A, 491, 157
- Rossi, E., et al. 2002, MNRAS, 332, 945
- Sakamoto, T., et al. 2004, ApJ, 602, 875
- Sakamoto, T., et al. 2005, ApJ, 629, 311
- Sakamoto, T., et al. 2008, ApJ, 679, 570
- Santana, R., et al. 2014, ApJ, 785, 29
- Sari, Re'em, Piran, Tsvi, & Halpern, J. P. 1999, ApJ, 519, 17
- Schlegel, D. J., Finkbeiner, D. P., Davis, M. et al. 1998, ApJ, 500, 525
- Soderberg, A. M., Kulkarni, S. R., Nakar, E., et al. 2006, Nature, 442, 1014
- Soderberg, A. M., et al. 2007, ApJ, 661, 982
- Spergel, D. N., Bean, R., Dor, O., et al. 2007, ApJS, 170, 377
- Tanvir, N. R., et al. 2009, Nature, 461, 1254
- Urata, Y., Huang, K., Yamazaki, R. et al. 2015, ApJ, 806, 222
- van Eerten, H., van der Horst, A., & MacFadyen, A. 2012, ApJ, 749, 44
- Wanderman, D., & Piran, T. 2010, MNRAS, 406, 1944
- Woosley, S. E., & Bloom, J. 2006, ARA&A, 44, 507
- Yamazaki, R., Ioka, K., & Nakamura, T. 2002, ApJ, 571, L31
- Yamazaki, R., Ioka, K., & Nakamura, T. 2003, ApJ, 593, 941
- Yamazaki, R., Ioka, K., & Nakamura, T. 2004, ApJ, 607, L103
- Yonetoku, D., Murakami, T., Nakamura, T., et al. 2004, ApJ, 609, 935
- Zhang, B., et al. 2006 ApJ, 642, 354